J. Fluid Mech. (2023), *vol*. 962, A3, doi:10.1017/jfm.2023.209

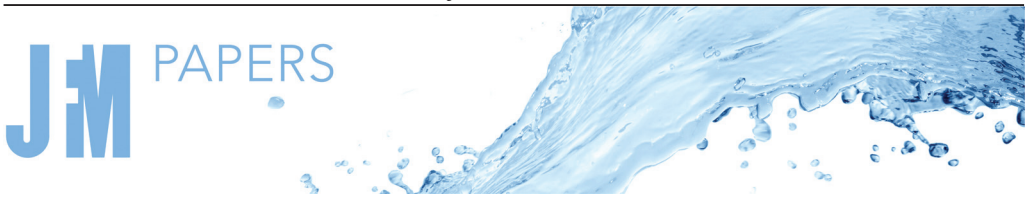

Thin disks falling in air

Amy Tinklenberg[1,2,†], **Michele Guala**[1,3] **and Filippo Coletti**[4]

[1]Saint Anthony Falls Laboratory, University of Minnesota, Minneapolis, MN 55414, USA

[2]Department of Aerospace Engineering and Mechanics, University of Minnesota, Minneapolis, MN 55455, USA

[3]Department of Civil, Environmental, and Geo- Engineering, University of Minnesota, Minneapolis, MN 55455, USA

[4]Department of Mechanical and Process Engineering, ETH Zürich, Switzerland

(Received 20 September 2022; revised 6 March 2023; accepted 6 March 2023)

We experimentally investigate the settling of millimetre-sized thin disks in quiescent air. The range of physical parameters is chosen to be relevant to plate crystals settling in the atmosphere: the diameter-to-thickness aspect ratio is $\chi = 25$–60, the Reynolds numbers based on the disk diameter and fall speed are $Re = O(10^2)$ and the inertia ratio is $I^* = O(1)$. Thousands of trajectories are reconstructed for each disk type by planar high-speed imaging, using the method developed by Baker & Coletti (*J. Fluid Mech.*, vol. 943, 2022, A27). Most disks either fall straight vertically with their maximum projected area normal to gravity or tumble while drifting laterally at an angle $< 20^\circ$. Two of the three disk sizes considered exhibit bimodal behaviour, with both non-tumbling and tumbling modes occurring with significant probabilities, which stresses the need for a statistical characterization of the process. The smaller disks (1 mm in diameter, $Re = 96$) have a stronger tendency to tumble than the larger disks (3 mm in diameter, $Re = 360$), at odds with the diffused notion that $Re = 100$ is a threshold below which falling disks remain horizontal. Larger fall speeds (and, thus, smaller drag coefficients) are found with respect to existing correlations based on experiments in liquids, demonstrating the role of the density ratio in setting the vertical velocity. The data supports a simple scaling of the rotational frequency based on the equilibrium between drag and gravity, which remains to be tested in further studies where disk thickness and density ratio are varied.

Key words: particle/fluid flow

† Email address for correspondence: tinkl014@umn.edu

1. Introduction

The primary motivation of the present work is the need for a predictive understanding of the settling of frozen precipitation, a fundamental natural process with deep ramifications. This is essential for improving the forecast of weather and snow accumulation on the ground (Hong, Dudhia & Chen 2004; Lehning *et al.* 2008). The parameterization of hydrometeor fall speed also influences the simulated properties of atmospheric clouds (Khvorostyanov & Curry 2002), which in turn are among the main sources of uncertainty in climate projections (Bodenschatz *et al.* 2010; IPCC 2021). Additionally, the orientation of ice particles is key to our understanding of polarimetric radar measurements for weather predictions and cloud monitoring (Radenz *et al.* 2019). The precipitation process is complicated by the wide variety of frozen hydrometeors present in different micro-physical conditions, resulting in a range of densities, sizes, shapes and velocities (Heymsfield & Westbrook 2010; Pruppacher & Klett 2010; Garrett & Yuter 2014; Nemes *et al.* 2017; Li *et al.* 2021).

Here we focus on plate crystals, which exhibit a remarkably simple shape (typically hexagonal) and represent a large fraction of all frozen hydrometeors in atmospheric clouds (Pruppacher & Klett 2010). Higuchi (1956) observed plates with diameters between 0.1–1.2 mm, the most probable being 0.75 mm. Kajikawa (1972) reported diameters ranging from 0.5−2 mm, aligned with the findings of Ono (1969). Auer & Veal (1970) collected plate crystals up to 3 mm in diameter. Less variability is observed for the plate thickness: Ono (1969) measured it to be up to 60 μm, while Kajikawa (1972) found it consistently near 50 μm. The density is typically taken as that of ice $\approx$917 kg m^{-3} (Jayaweera & Cottis 1969; Cheng, Wang & Hashino 2015). Measured terminal velocities of plate crystals show a spread from 0.5 m s^{-1} to over 2 m s^{-1}, with the variations for a given size of $\pm$0.3–0.7 m s^{-1} (Kajikawa 1972; Barthazy & Schefold 2006). These observations have informed empirical formulations to predict the crystal fall speed based on diameter, mass and/or projected area normal to the direction of fall (Böhm 1989; Heymsfield & Westbrook 2010; Tagliavini *et al.* 2021*a*).

It is often assumed that ice crystals maintain their direction of maximum extension approximately horizontal while settling (Sassen 1980; Matrosov *et al.* 2001; Wang 2021). A variety of other styles, however, have been observed for plate crystals, including oscillatory and tumbling motions (Kajikawa 1992; Mitchell 1996). Above a threshold level of the Reynolds number Re, the wake behind a free-falling object oscillates and produces unsteady loads, coupling the object motion and the wake itself (Ern *et al.* 2012; Mathai *et al.* 2018). Here $Re = V_t D/\nu$, where V_t is the terminal velocity, D is the plate diameter and ν is the air kinematic viscosity. Willmarth, Hawk & Harvey (1964) and List & Schemenauer (1971) reported a threshold $Re \approx 100$ for thin disks. The field observations cited above imply that Re for plate crystals can span two orders of magnitude ($Re \approx$ 5–500), suggesting a variety of possible falling style scenarios and sensitivity to environmental perturbations. In fact, the laboratory observations of falling crystals by Kajikawa (1992) indicated oscillatory motions as early as $Re \approx 40$.

The general problem of the falling behaviour of thin disks has attracted considerable attention. Due to the strong coupling between torque and drag, the dynamics are richer than for spheres (which also present a multiplicity of regimes; Jenny, Duek & Bouchet 2004; Zimmermann *et al.* 2011; Uhlmann & Doychev 2014; Mathai *et al.* 2016; Brandt & Coletti 2022; Raaghav, Poelma & Breugem 2022). In their seminal laboratory study, Willmarth *et al.* (1964) considered the parameter space defined by Re and the inertia ratio $I^* = I/(\rho_f D^5)$. The latter compares the disk's moment of inertia to that of the fluid sphere circumscribing it. For a circular disk of thickness h, $I^* = (\pi/64)\tilde{\rho}/\chi$, where $\tilde{\rho} = \rho_d/\rho_f$

is the disk-to-fluid density ratio and $\chi = D/h$ is the disk diameter-to-thickness aspect ratio. Three motion regimes were identified in non-overlapping regions of the $Re - I^*$ plane: stable (persistent horizontal orientation independent of initial conditions), fluttering (back and forth lateral oscillation), and tumbling (continuously turning end-over-end). Field *et al.* (1997) performed further experiments that distinguished between periodic and chaotic fluttering, the latter referring to oscillations with growing amplitudes until the disk overturns and tumbles above a critical inclination. During tumbling, the rotation-induced net lift leads to lateral drifting (Field *et al.* 1997; Mittal, Seshadri & Udaykumar 2004; Fabre, Assemat & Magnaudet 2011; Ern *et al.* 2012). A limitation of this parameter space is that Re is not an ideal control parameter, because V_t is an output quantity not known *a priori* (Mathai, Lohse & Sun 2020). Auguste, Magnaudet & Fabre (2013) described their numerical results via a regime map defined by I^* and the Archimedes number $Ar = \sqrt{(3/32)}U_g D/\nu$, where $U_g = \{2|\tilde{\rho} - 1|gh\}^{1/2}$ is the gravitational velocity (g being the gravitational acceleration). These authors also identified non-planar regimes involving a slow precession of the trajectory plane. Chrust, Bouchet & Dušek (2013) represented their computational findings using the non-dimensional disk mass m^* (which equals $16I^*$ for their infinitely thin disks) and the Galileo number $Ga = U_g D/\nu$. (Note that Ar and Ga only differ by the numerical prefactor, and that they have been used somewhat interchangeably in the literature; e.g. Ern *et al.* 2012.)

These numerical studies pointed out the bistability of certain ranges of the parameter space, i.e. the possibility that multiple falling modes may coexist. The behaviour of falling and rising disks and cylinders was mapped against Ga and I^* in various other studies, e.g. Namkoong, Yoo & Choi (2008), Mathai *et al.* (2017), Toupoint, Ern & Roig (2019).

Similar dynamics have also been investigated for rectangular plates/cards (Belmonte, Eisenberg & Moses 1998; Mahadevan, Ryu & Samuel 1999; Pesavento & Wang 2004; Andersen, Pesavento & Wang 2005; Jones & Shelley 2005; Eloy, Souilliez & Schouveiler 2007; Lau, Huang & Xu 2018). These studies, often motivated by flight mechanics and typically focused on the range $Re = O(10^2 - 10^3)$ and $I^* < 1$, indicated that a fluttering-to-tumbling transition occurs as I^* increases. However, for heavy plates with $I^* > 1$, experiments of Heisinger, Newton & Kanso (2014) and simulations of Lau *et al.* (2018) found that a quasi-steady descent is recovered in the limit of large I^*, as the object inertia dominates over the aerodynamic forces. Figure 1 depicts the $I^* - Ga$ regime map based on several of the above-mentioned studies and indicates the cases considered in the present paper, which are designed to be representative of plate crystals falling in the atmosphere.

The falling style influences the drag, lift and torque coefficients. Correlations linking the latter to the orientation of non-spherical objects have been proposed by Rosendahl (2000), Yin *et al.* (2003) and Zastawny *et al.* (2012). Recently, advanced formulations for estimating V_t (and the associated drag coefficient C_D) for realistic ice crystal shapes were proposed for fixed falling orientations (Tagliavini *et al.* 2021*a*,*b*). However, it is not trivial to determine the level of fluid inertia beyond which the wake becomes strongly coupled with the object motion (Auguste *et al.* 2013). Bagheri & Bonadonna (2016) highlighted the importance of the unsteady dynamics towards the terminal velocity, and McCorquodale & Westbrook (2021*b*) noted the onset of unsteady motions for thin disks resulted in a distinct change in the $C_D - Re$ relation. The net effect of the falling style on the fall speed over a broad range of parameters remains to be understood. Pesavento & Wang (2004) found tumbling plates to fall slower than gliding ones, while Bagheri & Bonadonna (2016) concluded that the rotation of non-spherical free-falling particles yields a faster descent by reducing the mean projected area.

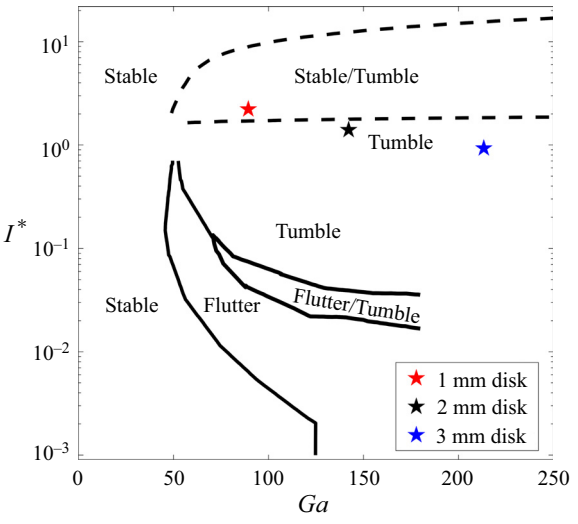

Figure 1. Disks in the current study placed among data from previous studies in the parameter space of the inertia ratio I^* versus Galileo number Ga. Solid black lines show the falling mode boundaries identified by Auguste *et al.* (2013). Dashed black lines indicate upper and lower boundaries of the region of bistability found by Lau *et al.* (2018). Red, black and blue stars indicate the 1, 2 and 3 mm disks used in this study, respectively. Data from other publications digitized using WebPlotDigitizer (Rohatgi 2021).

Even though often motivated by atmospheric precipitation, the vast majority of laboratory studies on falling thin disks have been carried out in liquid fluids (Willmarth *et al.* 1964; List & Schemenauer 1971; Jayaweera 1972; Field *et al.* 1997; Zhong, Chen & Lee 2011; Heisinger *et al.* 2014; Westbrook & Sephton 2017; Esteban, Shrimpton & Ganapathisubramani 2018, 2020; McCorquodale & Westbrook 2021*b*). This contradiction was clearly highlighted, for example, by Bagheri & Bonadonna (2016) in their review of previous work. *Re* similarity to atmospheric conditions is achieved by scaling up the object, which facilitates trajectory reconstruction and imaging of the wake. The concern with extending results at these low density ratios ($\tilde{\rho} \approx 1$) to frozen hydrometeors ($\tilde{\rho} \approx 1000$) is embodied by the different ranges of the inertia ratio: in those 'analogue experiments' it is typically $I^* = O(10^{-3}{-}10^{-2})$, while for plate crystals in the atmosphere, $I^* = O(1)$. In other words, as remarked by Westbrook & Sephton (2017), the invoked dynamic similarity (independent of $\tilde{\rho}$) is only valid when the wake oscillations are damped and the drag is not two-way coupled with the particle kinematics, such that the object falls steadily and the process is entirely controlled by *Re*. Additionally, most of the previous studies have reported results from a small number of realizations for each particle type, with limited information on their statistical variability, and in particular, on the occurrence frequency of various falling styles. Considerations on the bistability of certain regions of the parameter space, and in general the sensitivity to initial conditions, call for an analysis of the probability distributions of the important observables (Esteban *et al.* 2018; Lau *et al.* 2018).

In the present study, we investigate experimentally the dynamics of thin disks falling in quiescent air, with mass and size directly relevant to plate crystals settling in the atmosphere. We perform high-speed imaging and capture thousands of trajectories, analysing both translational and rotational motion. Our study pivots around some outstanding questions: Which falling style is predominant for disks of different sizes? How does the rotational–translational coupling affect the fall speed? What determines the time

Nominal diameter	D (mm)	h (μm)	χ	$\tilde{\rho}$	U_g (m s^{-1})	Ga	I^*
1 mm	1.27 ± 0.07	50 ± 7.5	25.4	1150	1.06	89.4	2.22
2 mm	2.02 ± 0.03	50 ± 7.5	40.4	1150	1.06	142.2	1.40
3 mm	3.03 ± 0.02	50 ± 7.5	60.6	1150	1.06	213.3	0.93

Table 1. Disk properties and relevant non-dimensional quantities based on the disk geometry and inertial properties. Here D is the measured mean disk diameter, h is the measured mean disk thickness, both D and h are listed with $\pm$ one standard deviation (σ) from measurements performed of these quantities. Also included are the diameter-to-thickness aspect ratio $\chi = D/h$, the density ratio $\tilde{\rho} = \rho_d/\rho_f$, the gravitational velocity $U_g = \{2|\tilde{\rho} - 1|gh\}^{1/2}$, the Galileo number $Ga = U_g D/\nu$ and the inertia ratio $I^* = (\pi/64)\tilde{\rho}/\chi$.

scale of the rotational motion? The paper is organized as follows. The methodology is presented in § 2, detailing the experimental apparatus and measurement procedure (§ 2.1), the image processing (§ 2.2) and uncertainty analysis (§ 2.3). Results are presented in § 3, with a demonstration of the observed falling styles in § 3.1, followed by the analysis of the translational dynamics in § 3.2 and rotational dynamics in § 3.3. In § 4, the results are further discussed, and the main conclusions are drawn.

2. Methodology

2.1. *Materials and experimental apparatus*

The utilized particles are solid, thin disks made of polyethylene terephthalate (PET) used for commercial glitter, with a density of $\rho_d = 1380$ kg m^{-3}. The disks settle in air at 20°C, with density $\rho_f = 1.2$ kg m^{-3}. Three disk sizes are considered, with nominal diameters of $D = 1$, 2 and 3 mm, all of thickness $h = 50$ μm. The dimensions of a subset of 30 disks per diameter are directly measured and yield the mean and standard deviations listed in table 1, along with the key physical parameters for each disk type. The diameters are obtained by imaging disks lying on a tray, while the thicknesses are obtained by tightening caliper teeth on stacks of various numbers of disks and calculating the average thickness in each stack, confirming the specification from the vendor.

The disks are imaged as they fall through a large, transparent chamber, about 2 m tall and 5 m^3 in volume (schematic shown in figure 2). The apparatus was designed to investigate the settling of particles in homogeneous turbulence and is described in detail in Carter *et al.* (2016) and Petersen, Baker & Coletti (2019). The experimental device, imaging system and processing approaches deployed in it have successfully reproduced established results and enabled novel findings on the statistics of the turbulence structure (Carter & Coletti 2017, 2018), clustering and settling velocity of spherical particles (Petersen *et al.* 2019), their dispersion and acceleration (Berk & Coletti 2021) and their two-way coupling with air turbulence. In the present study, no turbulence is forced, and the disks fall in otherwise quiescent air. A 3 m long cylindrical chute, 15.2 cm in diameter, is connected to an opening in the chamber ceiling and provides a fall distance of over 4 m from the release point to the imaging region approximately in the middle of the chamber. Based on the disk properties, previous studies and acceleration measurements, this is deemed amply sufficient for the terminal velocity to be attained, history effects from the release mechanism to be forgotten and the final falling styles to establish (Chrust *et al.* 2013; Heisinger *et al.* 2014; Esteban *et al.* 2020). The disks are dispensed using a sieve shaker (Gilson Performer III Model SS-3). A thick layer of disks fills the sieve at all times during the process, warranting steady operation and approximately constant spatial concentration

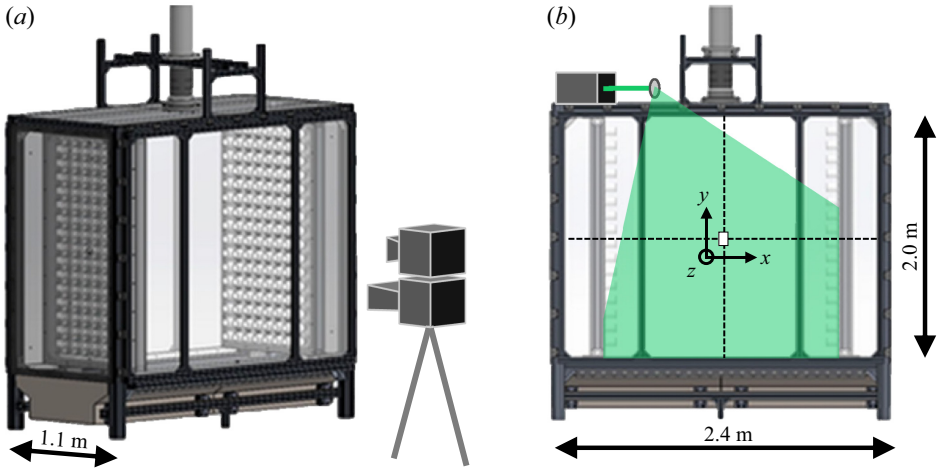

Figure 2. Facility schematic adapted from Carter *et al.* (2016). (*a*) Camera arrangement to capture both fields of view. (*b*) Laser sheet configuration and definition of global axes, with the imaging region centred in the chamber shown as a white rectangle.

in the imaging volume throughout the experimental runs (as verified by the imaging procedure described below). A volume fraction $\Phi_V \approx 10^{-5}$ is targeted, corresponding to a number density of $O(10^4$–$10^5)$ disks per cubic metre, depending on their size. This is comparable to concentrations of frozen hydrometeors reported in field studies (Lauber *et al.* 2021; Li *et al.* 2021) and warrants large enough inter-particle distance to prevent consequential interactions. While it cannot be excluded that individual trajectories are affected by the presence of nearby wakes, these are expected to have a minor influence on the statistics of the large number of trajectories we report. This is verified by performing measurements at reduced concentrations ($\Phi_V \approx 10^{-6}$), leading to analogous results and conclusions (see the Appendix). We note that the mean inter-disk distance ranges between 11 and 15 diameters for $\Phi_V \approx 10^{-5}$, and between 24 and 31 diameters for $\Phi_V \approx 10^{-6}$.

A high-speed Nd:YLF laser (Photonics, 30 mJ pulse^{-1}) operated at 4300 Hz is used along with a combination of one cylindrical and two spherical lenses to form a $\sim$3 mm-thick light sheet. This is shined through the transparent ceiling to illuminate a vertical plane about the centre of the chamber under the chute opening. The illuminated plane is associated to x, y and z coordinates in the horizontal, vertical upward and out-of-plane direction, respectively, and is imaged by two high-speed CMOS cameras (Phantom VEO 640) synchronized with the laser. Different objectives are used on each camera: a 105 mm Nikon lens for a larger field of view (LFV), and a 200 mm Nikon lens for a smaller field of view (SFV), nested within the LFV. Images are taken at a resolution of 1280 $\times$ 960 pixels, such that the LFV is 11.2×8.4 cm^2 with 11.4 pixels mm^{-1}, and the SFV is 4.8×3.6 cm^2 with 26.6 pixels mm^{-1}. The dual imaging set-up extends the dynamic range of the measurements: the LFV captures longer and more numerous trajectories, while the higher resolution of the SFV enables more accurate reconstruction of the translational and rotational kinematics. All statistics obtained from the LFV are effectively indistinguishable to those from SFV, indicating that the disk motions in the imaging plane are reconstructed with sufficient resolution. We will therefore report results from the LFV only. A minimum of five experimental runs is performed for each disk type, with each run lasting approximately 10 s.

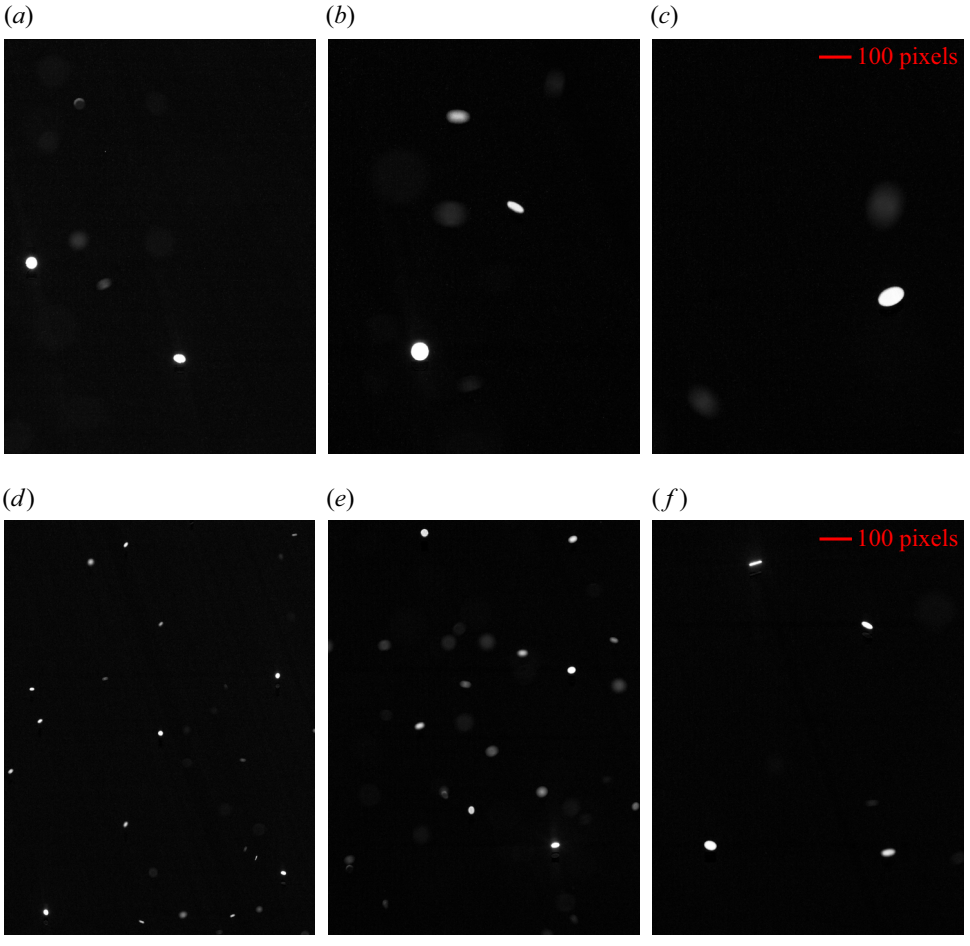

Figure 3. Sample images from measurements. Snapshots (*a*) to (*c*) shown at increasing disk diameter for the smaller FOV; (*d*) to (*f*) are for the larger FOV. For reference, a scale bar of 100 pixels is also shown.

2.2. *Reconstruction of the disk trajectories*

Background subtraction is first applied to the raw images based on the per-pixel minimum intensity across each run. Example raw images are shown in figure 3. An intensity threshold is then applied to identify all disks in the field of view. These are bright due to the glitter's shiny finish; thus, the number of identified objects is practically insensitive to the exact threshold. We then remove out-of-focus objects via additional thresholding based on size and sharpness. At the present resolution, even the smaller disks have diameters of $\sim$14 pixels in the LFV; thus, the size-based thresholding is straightforward. For the sharpness, we use the Sobel approximation to compute the intensity gradients within each object, with components G_x and G_y. The variance of $|G_xG_y|$ from all pixels defines the object sharpness. The threshold on the latter is set based on visual inspection of tens of disks, and its precise value has no appreciable influence on the statistics we will present.

Measured properties of the imaged disks include their centroid position (x_0, y_0), the major and minor axis lengths of the ellipse best fit to the particle image (d_M and d_m), and the orientation of the major axis off the horizontal (θ); see figure 4(*a*). The disks' shiny finish causes a slight glare and, therefore, they appear thicker than their actual

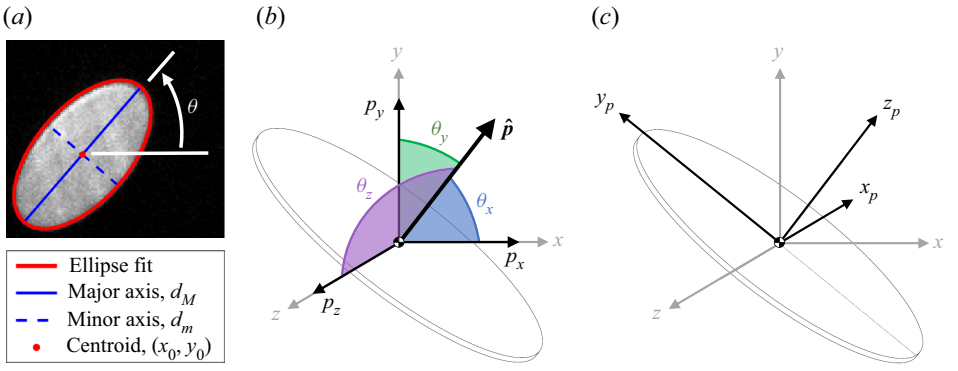

Figure 4. (*a*) A 3 mm disk image example with ellipse fit and measured properties from the disk detection. (*b*) Disk orientation vector, $\hat{\boldsymbol{p}}$, and its components shown in black. Global axes are shown in grey. Relative angles between $\hat{\boldsymbol{p}}$ and each of the global axes are shown with coloured arcs. (*c*) Axes in the reference frame of the disk shown in black, relative to the global axes in grey.

physical dimension. For this reason, following Baker & Coletti (2022), a shift of $-\delta d_m$ is applied to the measured distribution of d_m to retrieve the known size range.

To reconstruct the disk trajectories, a nearest-neighbour in-house PTV algorithm is applied to track the object centroids. At the present spatio-temporal resolution, the disk frame-to-frame movement is typically about 3.0–4.8 pixels or $0.21D$–$0.14D$, which leaves no ambiguity in tracking the sparse objects. To reduce unavoidable noise due to the finite resolution and accuracy, a Gaussian filtering procedure is applied to the trajectories. The temporal kernel τ_k is chosen as the smallest value beyond which the acceleration variance decays exponentially. Such a procedure, originally proposed by Voth *et al.* (2002), has been applied by several groups to both tracers and heavy particles (Mordant, Crawford & Bodenschatz 2004*a*; Gerashchenko *et al.* 2008; Ebrahimian, Sean Sanders & Ghaemi 2019), and extensively by our group to spherical particles in air (Berk & Coletti 2021) and in water (Baker 2021), snow and ice particles in the atmosphere (Nemes *et al.* 2017; Li *et al.* 2021), and recently non-spherical particles (Baker & Coletti 2022). We adopt $\tau_k = 3.95$ ms or 17 image frames for all disks, which is an order of magnitude smaller than the characteristic tumbling period; see § 3.3.

The imaged trajectories are two-dimensional (2-D) projections of the three-dimensional (3-D) trajectories along the x–y imaging plane. In the present regime with relatively large fall speeds, all imaged trajectories in the field of view are closely approximated by straight lines, with an average correlation coefficient typically larger than 0.95. While the reconstructed trajectories are curvilinear, the linear best fit allows for definition of a single inclination angle for each trajectory. We denote with ψ the angle between a 3-D trajectory and the vertical, and with ϕ the corresponding angle of its 2-D projection. While the 2-D imaging approach directly measures ϕ, in § 3.2 we shall see how one can estimate ψ via reasonable assumptions on the rotational dynamics.

The values of θ and d_m are used to determine the instantaneous 3-D orientation along each trajectory, relying on the known disk geometry and the relatively high spatial resolution, following the approach recently introduced by Baker & Coletti (2022). The components of the unit vector $\hat{\boldsymbol{p}} = [p_x\ p_y\ p_z]$ aligned with the disk's axis of rotational

symmetry (figure 4*b*) are calculated as

$$p_x = \cos(\theta_x) = \sin(\theta)\sqrt{1 - \left(\frac{d_m - \delta d_m}{D}\right)^2}, \tag{2.1}$$

$$p_y = \cos(\theta_y) = \cos(\theta)\sqrt{1 - \left(\frac{d_m - \delta d_m}{D}\right)^2} * -\text{sign}(\theta), \tag{2.2}$$

$$p_z = \cos(\theta_z) = \frac{d_m - \delta d_m}{D}. \tag{2.3}$$

Figure 4(*c*) depicts the coordinate axes attached to the frame of reference of the disk, with z_p aligned with $\hat{\boldsymbol{p}}$ by construction. Tumbling is defined as the edge-over-edge rotation, i.e. with the rotation vector $\boldsymbol{\omega}$ perpendicular to $\hat{\boldsymbol{p}}$; while spinning is defined as rotation about z_p, i.e. with $\boldsymbol{\omega}$ parallel to $\hat{\boldsymbol{p}}$ (Voth & Soldati 2017). In our planar imaging, x_p and y_p are indistinguishable and only tumbling can be measured. As for the translational motion, Gaussian filtering is applied to calculate the first and second derivatives of the orientation vector, $\dot{\hat{\boldsymbol{p}}} = \partial\hat{\boldsymbol{p}}/\partial t$ and $\ddot{\hat{\boldsymbol{p}}} = \partial^2\hat{\boldsymbol{p}}/\partial t^2$, obtaining the tumbling angular velocity $\boldsymbol{\omega_t}$ and tumbling angular acceleration $\boldsymbol{\alpha_t}$,

$$\boldsymbol{\omega_t} = [\omega_x\ \omega_y\ \omega_z] = \hat{\boldsymbol{p}} \times \dot{\hat{\boldsymbol{p}}}, \tag{2.4}$$

$$\boldsymbol{\alpha_t} = [\alpha_x\ \alpha_y\ \alpha_z] = \dot{\hat{\boldsymbol{p}}} \times \ddot{\hat{\boldsymbol{p}}}. \tag{2.5}$$

Considering the angular acceleration variance as a function of the Gaussian temporal kernel, the same value of τ_k used for the translational motion is found appropriate also for the rotational motion. This is consonant with the notion that the rotational and translational response times of non-spherical particles are typically of the same order (Voth & Soldati 2017).

The Gaussian filtering imposes a lower limit τ_k on the temporal duration of the trajectories. Moreover, only trajectories contained within the $\sim$3 mm-thick illuminated volume are reconstructed. As we shall see, the tracked disks fall at an angle smaller than $\sim 20^\circ$ from the vertical. Based on the measured velocities, even a tumbling disk that drifts precisely in the z direction will spend about 5 ms ($\sim 1.3\tau_k$) in the illuminated volume, sufficient for the trajectory to be reconstructed. Thus, the results we present are not expected to be overshadowed by selection bias.

The present dataset consists of 29 554 trajectories for the 1 mm disks, 10 817 trajectories for the 2 mm disks and 1118 trajectories for the 3 mm disks. We will denote with an overbar trajectory-averaged quantities (that is, quantities that are averaged along each disk trajectory), while an angle bracket will indicate global averaging across all instantaneous events. An example of a reconstructed trajectory for a tumbling 3 mm disk is shown in figure 5, along with plots of its main kinematic descriptors. Following the above-mentioned coordinate system, negative vertical components of velocity and acceleration are in the downward direction. The periodicity of the motion is apparent, as well as the lateral drift associated to tumbling.

2.3. *Uncertainty analysis*

The uncertainty associated with measured quantities is estimated through synthetic trajectory analysis following the method of Baker & Coletti (2022). Real disk images from the experiment are used to create a template for each disk size, where one quadrant

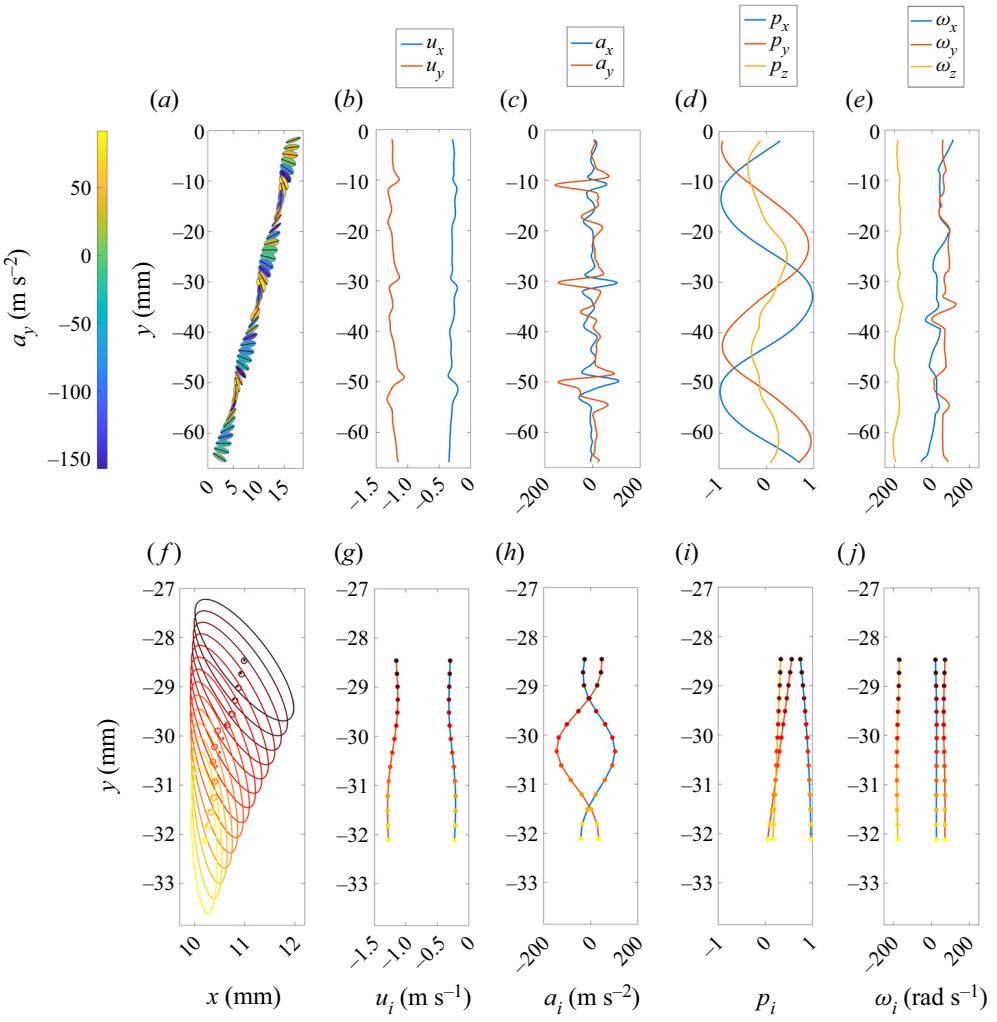

Figure 5. Processing result example for a single 3 mm trajectory, showing values along the trajectory including: (*a*) ellipse fit with centroid (red) and major axis (black) shown every 1.16×10^{-3} s, coloured by instantaneous vertical acceleration a_y; (*b*) horizontal velocity u_x and vertical velocity u_y; (*c*) horizontal acceleration a_x and vertical acceleration a_y; (*d*) orientation vector components; and (*e*) angular velocity components. (*f–j*) Portion of the same trajectory from (*a–e*) shown every 2.33×10^{-4} s, demonstrating the true temporal resolution and frame-to-frame centroid displacement of the experimental data at 4300 Hz. In (*f*), smoothed ellipse fits with open circles indicating detected disk centroids and solid points corresponding to the centroid trajectory after implementation of the Gaussian smoothing kernel. Coloured in time with corresponding data points across (*g–j*). Both u_y and a_y are taken positive upwards as shown in figure 4.

of the real disk is mirrored and stretched to achieve a symmetric geometry with an exactly known centroid and diameter. These templates are placed on a representative background extracted from the experimental data. A time sequence of images is generated with imposed velocities, accelerations, falling styles and rotation rates comparable to those in the experiments. Specifically, a constant angular velocity of 200 rad s^{-1} and a constant linear acceleration g is imposed. A Gaussian filtering procedure is applied to the centroid trajectories, analogous to the one used for the measurement data: the positions

Quantity	1 mm	2 mm	3 mm
x, y	0.01 mm, 0.7 %	0.01 mm, 0.7 %	0.02 mm, 0.5 %
u_x, u_y	0.01 m s^{-1}, 2.1 %	0.01 m s^{-1}, 1.2 %	0.01 m s^{-1}, 1.7 %
a_x, a_y	5.4 m s^{-2}, 37.1 %	5.6 m s^{-2}, 23.7 %	6.8 m s^{-2}, 20.0 %
p_x, p_y, p_z	0.04, 9.6 %	0.04, 7.0 %	0.02, 3.4 %
$\omega_x, \omega_y, \omega_z$	17.3 rad s^{-1}, 22.9 %	16.1 rad s^{-1}, 16.1 %	7.7 rad s^{-1}, 13.0 %

Table 2. Measurement uncertainty on the disk centroid location, velocity, acceleration, orientation and angular velocity for each disk size. Listed as dimensional quantities and as a percentage of the characteristic value from experimental data. For the centroid location (x, y), the characteristic value is taken as the diameter D.

are convolved with the first and second derivative of the chosen Gaussian kernel to obtain velocities and accelerations, respectively. The synthetic images are then processed using the same method as the experimental data by performing disk detection, trajectory reconstruction and orientation measurement. Five independent synthetic trajectories of various falling styles and dominant rotation directions are generated for each disk size, yielding $O(10^3)$ instantaneous realizations. The estimated errors for each quantity, listed in table 2, are calculated as the root-mean-square (r.m.s.) difference between the reconstructed and the prescribed values. Percentage errors are calculated by comparison with the r.m.s. value of the respective quantities from the experimental data. The errors in the acceleration and angular velocity are sizeable, but will not alter the conclusions.

3. Results

3.1. *Falling styles*

Figure 6 illustrates examples of different falling styles observed for the 3 mm disks. In the classifications of Field *et al.* (1997), these correspond to the stable mode (figure 6*a*), fluttering mode (figures 6(*b*) and 6(*c*), oscillating with smaller and larger amplitudes, respectively) and the tumbling mode (figure 6*d*). In order to identify the falling style, we quantify the angular excursion Δp_y, defined as the range of p_y values spanned by a disk during its trajectory. Only trajectories long enough to allow for a full tumble sequence are considered in this statistic. Ideally, for steadily falling disks, $\Delta p_y = 0$, while for tumbling disks, $\Delta p_y = 2$ (assuming the trajectories are contained in a vertical plane, thus, with excursions between $p_y = -1$ and $p_y = 1$); in reality, such limits are only approached. For fluttering, intermediate values of Δp_y are expected depending on the maximum inclination angle. This quantity captures tumbling in any direction using a single value per trajectory and yields similar results to those found using Δp_x. Figure 7 presents histograms of Δp_y for the three considered disk sizes. A bimodal distribution is observed for the 1 and 3 mm disks, while for the 2 mm disks, high values of Δp_y dominate. The distributions do not suggest a clear threshold to define fluttering. This is especially elusive because, in the present range of physical parameters, the lateral excursions typically associated to this mode are too small to be reliably detected. Therefore, in the following we will simply denote the trajectories as 'non-tumbling' and 'tumbling' based on whether Δp_y is smaller or larger than 1.5, respectively. It is clear from figure 7 that the exact value of the threshold is inconsequential for such definition. We note that the bimodal behaviour of the 1 mm disks and the consistent tumbling of the 2 mm disks agree with the regime map proposed by Lau *et al.* (2018) (see figure 1). However, the same map also predicts the 3 mm disks would always tumble, which is at odds with the present observations.

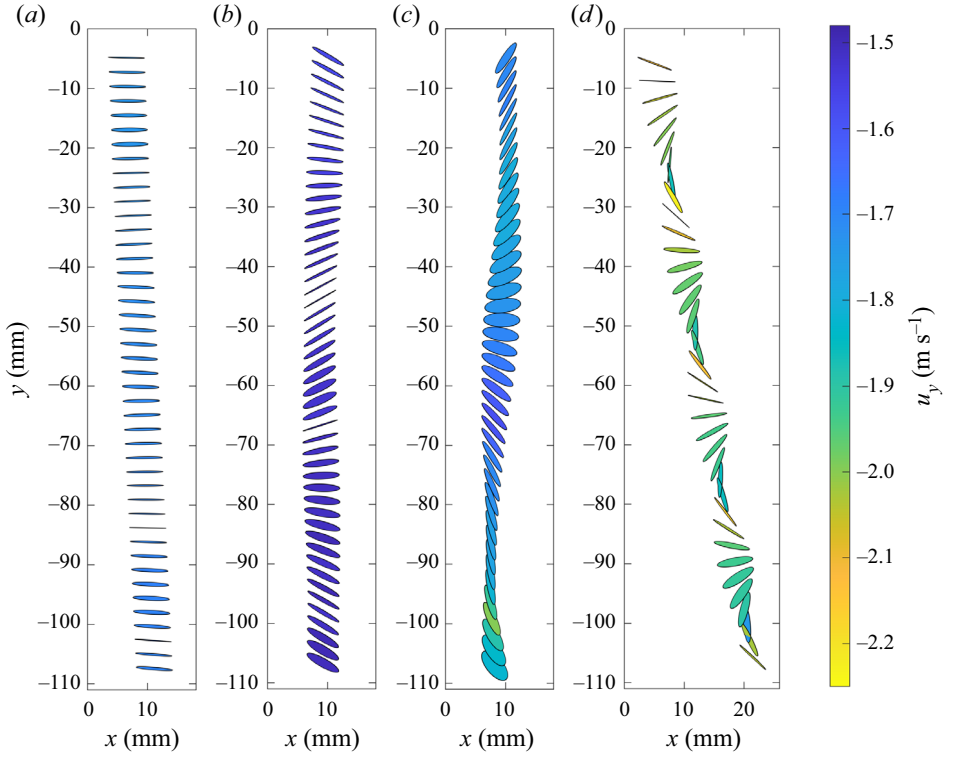

Figure 6. Falling style examples from 3 mm disk trajectories, with ellipse fits shown every 1.14×10^{-3} s. Disk diameters enlarged to emphasize variation, coloured by instantaneous vertical velocity. Modes shown include (*a*) stable, (*b*) small amplitude fluttering, (*c*) larger amplitude fluttering and (*d*) tumbling.

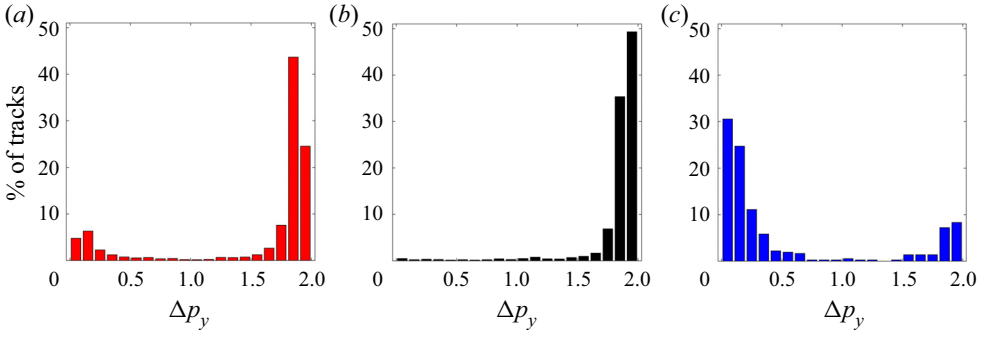

Figure 7. Histograms of p_y range along individual trajectories, shown as a percentage of trajectories for the (*a*) 1 mm, (*b*) 2 mm and (*c*) 3 mm disks.

The non-tumbling disks favour approximately horizontal orientations, maximizing their projected area in the vertical direction. This is demonstrated in figure 8, where the probability distribution functions (PDFs) of $|p_y|$, are plotted for the 1 and 3 mm disks and for both falling styles. (The 2 mm disks do not exhibit a statistically significant number of non-tumbling trajectories.) The axis of rotational symmetry of the non-tumbling disks is preferentially aligned to the vertical, while instances of non-tumbling disks falling edge-on are negligibly scarce.

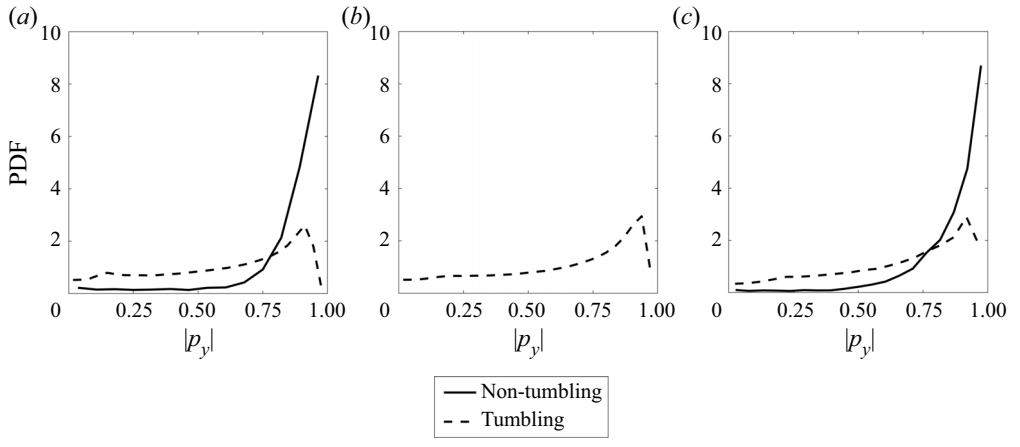

Figure 8. Distributions of the modulus of disk orientation vector vertical component p_y, separated by falling style family. Solid lines indicate non-tumbling and dashed lines indicate tumbling, for the (*a*) 1 mm, (*b*) 2 mm and (*c*) 3 mm disks. Here, $p_y = 1$ represents a perfectly flat orientation, while $p_y = 0$ represents edge-on orientation.

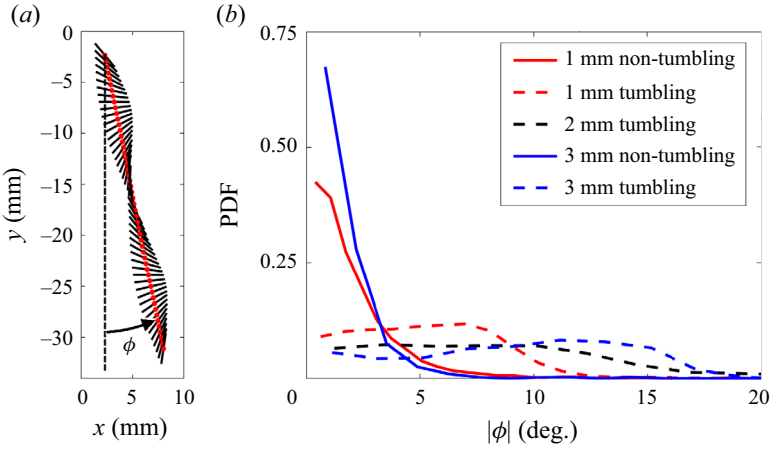

Figure 9. (*a*) Counterclockwise-rotating 1 mm disk major axis shown in black every 4.65×10^{-4} s. Major axis length enlarged to emphasize rotation direction of the disk. Inclination angle ϕ of linear fit to red centroid trajectory defined from dashed vertical line. (*b*) Distributions of the absolute value of trajectory inclination angles separated by falling style, where solid lines are used for the non-tumbling disks and dashed are used for the tumbling disks.

The tumbling disks are observed to drift laterally, in agreement with previous studies of thin falling bodies (Ern *et al.* 2012). Figure 9(*a*) illustrates a sample trajectory for a 1 mm tumbling disk, with the distributions of ϕ for the different cases shown in figure 9(*b*). While non-tumbling disks tend to fall with quasi-vertical trajectories, tumbling ones reach up to $\sim 12^\circ$ and 20° for the smaller and larger diameters, respectively. The broadness of the distributions largely depends on the imaged trajectories being 2-D projections of the 3-D trajectories, as illustrated in figure 10(*a*). Indeed, the angle ψ between the 3-D trajectories and the vertical is related to the projection angle ϕ by

$$\psi = \operatorname{atan}\left(\frac{\tan\phi}{\cos\gamma}\right), \tag{3.1}$$

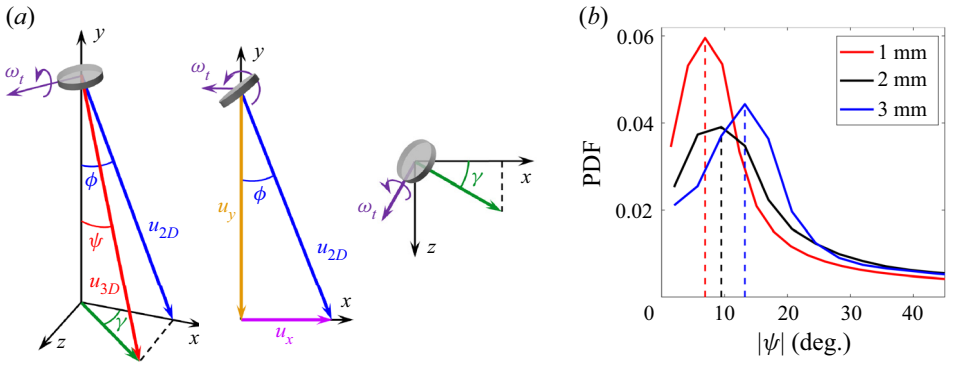

Figure 10. (*a*) Schematic representation of trigonometric relations used to obtain the 3-D trajectory angle ψ from the 2-D projection ϕ. (*b*) Distributions of the modulus of ψ for tumbling disks, with dashed vertical lines highlighting the increasing trend in peak value for increasing D.

where γ is the angle between the plane containing the 3-D trajectory and the x–y imaging plane. Under the standard assumption that the lateral drift is caused mainly by a rotation-induced lift in the direction of $\omega_t \times u$ (where u is the translational velocity; e.g. Belmonte *et al.* 1998; Fabre *et al.* 2011), we have

$$\cos\gamma = \frac{\overline{\omega_z}}{|\omega_t|}, \tag{3.2}$$

$$\psi = \operatorname{atan}\left(\frac{\dfrac{\tan\phi}{\overline{\omega_z}}}{\overline{|\omega_t|}}\right). \tag{3.3}$$

The PDF of ψ for the different cases in figure 10(*b*) clearly shows that the larger disks experience a stronger lateral drift, which is expected under larger circulation. The inclination from the vertical, however, is typically smaller than 20°, implying that the lift is subdominant with respect to the drag. This is in contrast with the tumbling plates studied by Belmonte *et al.* (1998), Mahadevan *et al.* (1999) and Andersen *et al.* (2005), which had lift-to-drag ratios close to unity and fell along directions close to 45° from the vertical. The difference is likely due to the smaller inertia ratio in those studies, $I^* = O(10^{-1}\text{–}10^{-2})$; in the present case the moment of inertia of the surrounding fluid is relatively smaller and, thus, the coupling of rotational and translation motion (driven by the shedding of vortices at various angles of attack; see Andersen *et al.* 2005) is less strong. This view is consistent with our observation that ψ increases for larger disks, which have smaller I^*.

3.2. *Translational dynamics*

We begin by plotting the terminal velocity $V_t = -\langle u_y \rangle$ versus the disk diameter in figure 11. The error bars, calculated with the conservative assumption that the number of independent samples coincide with the number of experimental runs, are comparable to the symbol size in these and other logarithmic plots. They will be shown later, however, when reporting the Reynolds number and drag coefficient. Superposing the data points with trend lines for various types of frozen hydrometeors reported by Kajikawa (1972) confirms a behaviour in line with plate crystals. The PDFs of the horizontal and vertical velocity components, u_x and u_y, respectively, are plotted in figure 12 normalized by V_t. The statistics of the vertical velocities are reported in table 3, with mean and

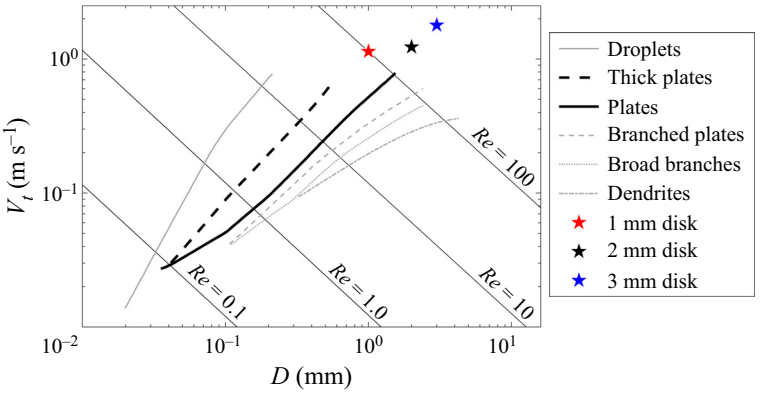

Figure 11. Measured V_t values for disks in the current study compared with settling velocities of several plate crystal hydrometeor varieties. Red, black and blue stars represent the 1, 2 and 3 mm disks, respectively. Figure adapted from Sassen (1980), with data for thick plates, plates and broad branches from Kajikawa (1972) and for branched plates and dendrites from Kajikawa (1975). Data from other publications digitized using WebPlotDigitizer (Rohatgi 2021).

standard deviations consistent with the observations of frozen hydrometeors (Kajikawa 1972; Barthazy & Schefold 2006). For comparison, Gaussian distributions are also shown. These provide reasonable approximations of the u_x distributions, while u_y display strong skewness with high probability of large instantaneous fall speeds. Similar skewness of the vertical velocity was found for both rising and falling particles, but at volume fractions where the wake-mediated interaction between particles was significant (Riboux, Risso & Legendre 2010; Huisman *et al.* 2016; Alméras *et al.* 2017; Fornari, Ardekani & Brandt 2018; Risso 2018). As in those cases, here the skewness can be associated to the entrainment of the flow in the object's wake (Riboux *et al.* 2010): larger downward fluctuations are more probable due to the rapid entrainment of ambient fluid in the wake of the falling disks that reduce the pressure difference between leading and trailing edges along with the instantaneous drag. Moreover, the coupling between translational and rotational motion (peculiar to the present case with large particle anisotropy) also plays a role: when the rotating disk is oriented edge-on, the small frontal area supports limited aerodynamic drag to contrast gravity, leading to larger downward velocities sustained by the particle inertia. This point will be further discussed in the following section. Recently, Moriche, Uhlmann & Dušek (2021) looked at individual oblate spheroids falling in quiescent fluid and also found skewness towards larger downward vertical velocities for particles with $\chi = 1.5$. A direct comparison to their results, however, is hampered by the different aspect ratios and density ratios.

Common non-dimensional parameters used to describe the mean fall speed are listed in table 3, including the drag coefficient $C_D = 2mg/(\rho_f A V_t^2)$ and the Best number $X = C_D Re^2$. Here, a classic formulation for C_D is used that assumes equilibrium between gravity and steady drag on a flat falling disk offering the maximum projected frontal area $A = \pi D^2/4$. To explore the effect of orientation, we also define an instantaneous drag coefficient based on the instantaneous projected frontal area A_{inst} and the simultaneous vertical velocity u_y, $C_{D,inst} = 2mg/(\rho_f A_{inst} u_y^2)$. The PDFs of $C_{D,inst}$ in figure 13 exhibit long tails, reflecting the skewness of u_y and the variability of A_{inst}. The dominant modes of the distributions are very close to C_D, indicating that the latter does provide a reasonable mean value representing the ensemble behaviour of all particle types.

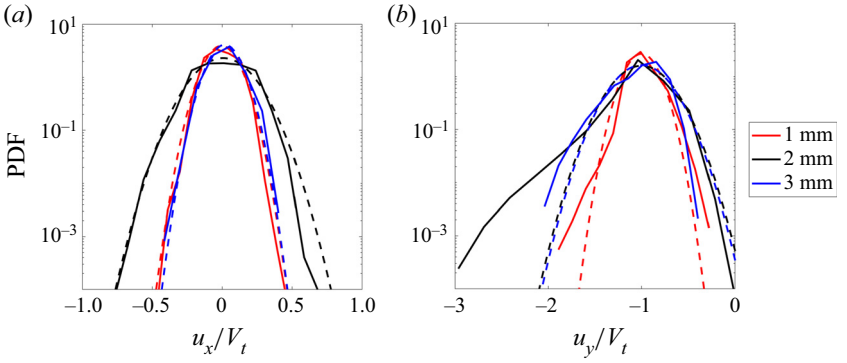

Figure 12. Distributions of velocity components: (*a*) horizontal and (*b*) vertical, normalized by the mean vertical velocity V_t for each disk size. Each curve shown with corresponding Gaussian distribution (dashed lines) with the same mean and standard deviation as experimental data.

Disk	V_t (m s^{-1})	Re	C_D	X
1 mm	1.14 ± 0.17	96.2	0.86	7998
2 mm	1.23 ± 0.31	165.0	0.74	20 234
3 mm	1.79 ± 0.44	360.1	0.35	45 526

Table 3. Disk terminal (vertical) velocities measured in quiescent air, shown with $\pm\sigma$. Other quantities shown include the Reynolds number, drag coefficient and Best number, all calculated from the mean V_t for each disk size.

Figure 14 compares the observed mean fall speeds with previous laboratory results. In figure 14(*a*) we plot Re versus Ga, along with the relation $Re = Ga$ (implying $V_t = U_g$) and the empirical relation obtained by Brown & Lawler (2003) (and reformulated in terms of Re and Ga by Cabrera 2021) for spheres. As U_g is the terminal velocity of a flat falling disk with unitary drag coefficient, Re becoming increasingly larger than Ga reflects the drop of C_D with increasing disk diameter. Despite the present particles being far from spherical, the agreement with Brown & Lawler (2003) is fair for the 1 and 2 mm disks. Figures 14(*b*) and 14(*c*) plot Re versus X and C_D versus Re, respectively, comparing with several previous studies on disks falling in liquid fluids. The agreement deteriorates with increasing diameter (and, thus, with Re). Figure 14(*d*), on the other hand, shows that our results are consistent with the findings of Bagheri & Bonadonna (2016). These authors proposed a rescaling of the data by the shape-dependent parameters k_S and k_N in the Stokesian and Newtonian drag regimes, respectively; see Bagheri & Bonadonna (2016) for definitions. Importantly, the higher-Re data in their study were obtained in air, thus, at density ratios similarly high as in the present study.

The falling style is directly connected to the aerodynamic drag, and thus, it is expected to influence the fall speed. In figure 15 we display the PDFs of the instantaneous vertical velocities, separating between non-tumbling and tumbling trajectories. The tumbling 1 mm disks fall measurably faster compared with the non-tumbling ones, while the opposite is true for the 3 mm particles. The reason for this different behaviour is unclear. We note, however, that such a difference in settling velocity is smaller than the width of the distributions.

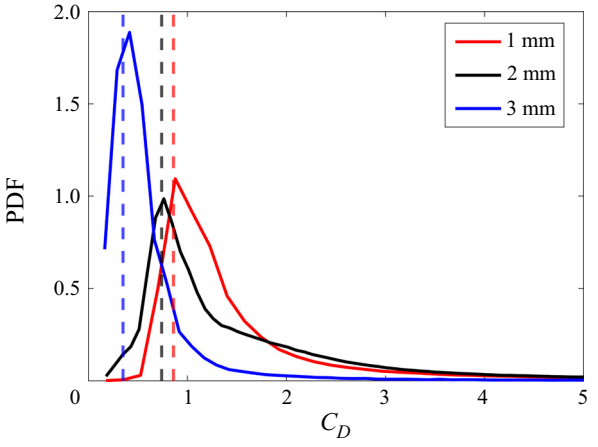

Figure 13. Distributions of the instantaneous drag coefficient calculated as $C_{D,inst} = 2mg/\rho_f A_{inst} u_y^2$ from the instantaneous projected area of the disks in the vertical direction and the instantaneous vertical velocity. Vertical dashed lines show the (nominal) drag coefficients calculated as $C_D = 2mg/\rho_f A V_t^2$ using the maximum disk projected area and the mean terminal velocity.

Further insight into the translational dynamics is provided by the PDFs of the disk linear accelerations, displayed in figure 16. The mean of both horizontal and vertical components is close to zero, as expected for free-falling objects that have reached terminal velocity. Compared with Gaussian distributions, both components are highly intermittent, with a non-negligible probability of reaching tens of g's. Observations of individual realizations and joint statistics of acceleration and number density, not shown for brevity, confirm that these extreme events are not related to mutual interactions between disks. The vertical components are also strongly skewed, i.e. the probability of reaching very large downward accelerations is even higher. Both the skewness and the kurtosis of the distributions increase with increasing disk size: as the object inertia increases, the instantaneous imbalance between gravity and drag can lead to extreme accelerations, especially in the downward direction ($a_y < 0$).

The inspection of individual trajectories indicates that such extreme acceleration events are associated to phases of the motion in which the disks fall edge-on (see figure 5). This is confirmed by figure 17, which displays distributions of the instantaneous vertical accelerations (here normalized by their r.m.s. values). The results are sorted in ranges of $|p_y|$, highlighting the differences between various orientations: when disks fall edge-on, the magnitude of the instantaneous accelerations are larger and more intermittent. Additionally, the distributions are more skewed, with relatively high probability of extreme downward accelerations. This confirms that instantaneous variability in the vertical acceleration is intrinsically related to the falling style, and to tumbling in particular.

3.3. *Rotational dynamics*

In order to quantify the disks' angular velocity, we first consider the trajectory-averaged magnitude, $\overline{|\omega_t|}$. Figure 18 shows joint PDFs (JPDFs) of $\overline{|\omega_t|}$ and the angular excursion Δp_y. Similarly to the histograms of Δp_y in figure 7, the 1 and 3 mm disks exhibit a bimodal behaviour: the tumbling disks ($\Delta p_y > 1.5$) have angular velocities around 200 rad s^{-1}, while rotation rates are an order of magnitude smaller for non-tumbling ones. Although a

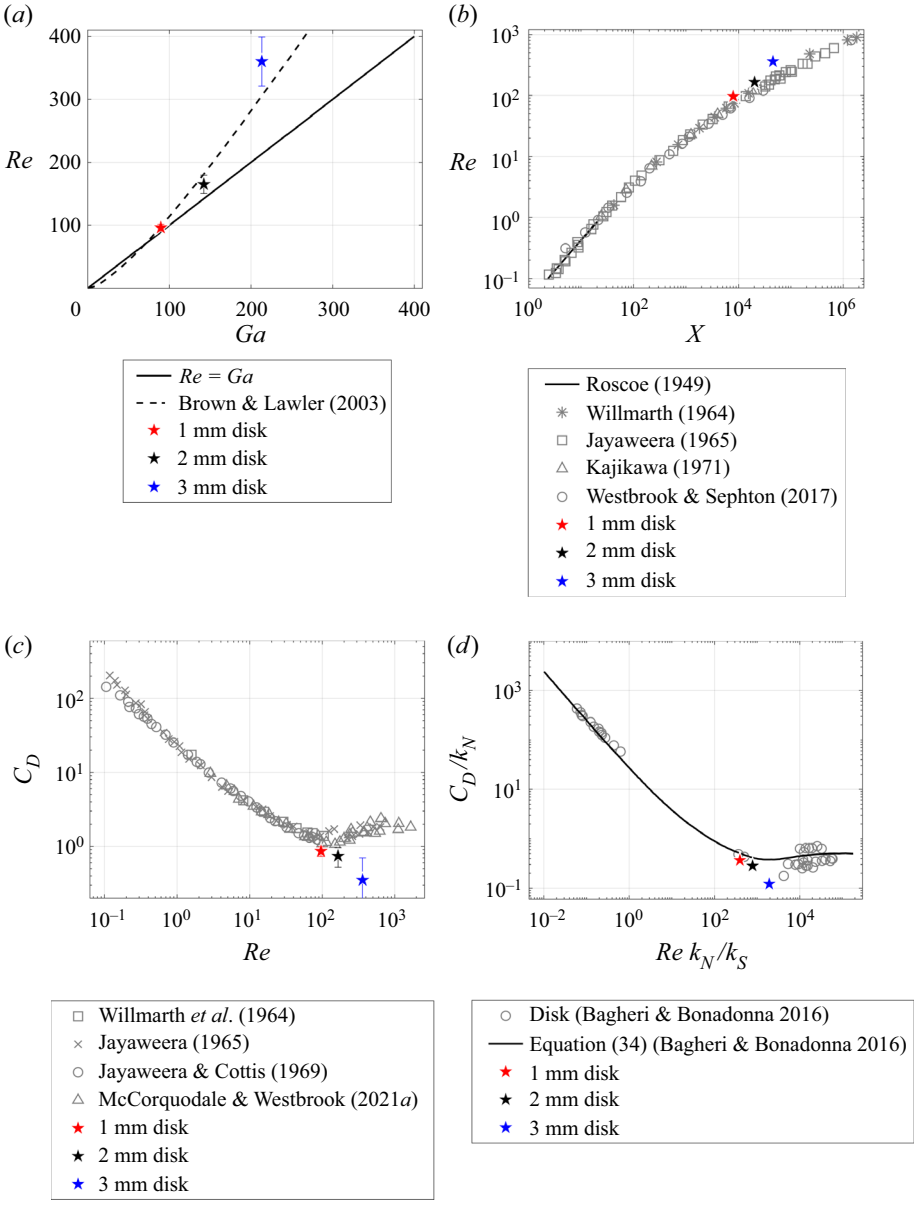

Figure 14. Red, black and blue stars represent the 1, 2 and 3 mm disks, respectively, in each of the following: (*a*) Reynolds number versus Galileo number with the solid black line of $Re = Ga$ implying $C_D = 1$. Empirical relation from Brown & Lawler (2003) (and reformulated by Cabrera 2021) shown in the black dashed line. (*b*) Westbrook & Sephton (2017) plot of Reynolds number versus Best number, including data from Roscoe (1949), Willmarth *et al.* (1964), Jayaweera (1965) and Kajikawa (1971). (*c*) McCorquodale & Westbrook (2021*a*) plot of drag coefficient versus Reynolds number, including data from Willmarth *et al.* (1964), Jayaweera (1965) and Jayaweera & Cottis (1969). (*d*) Bagheri & Bonadonna (2016) plot of corrected drag coefficient versus corrected Reynolds number, accounting for shape factors of particles such as elongation and flatness as well as density ratio between the particle and fluid. Data from other publications digitized using WebPlotDigitizer (Rohatgi 2021).

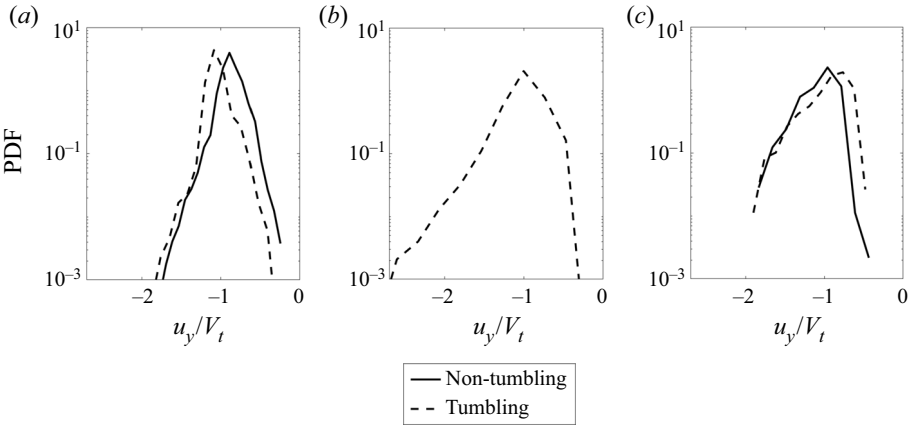

Figure 15. Instantaneous vertical velocity distributions normalized by terminal velocity. Separated by falling style, with non-tumbling shown in solid lines and tumbling shown with dashed lines for the (*a*) 1 mm, (*b*) 2 mm and (*c*) 3 mm disks. Negative values indicate downward velocities.

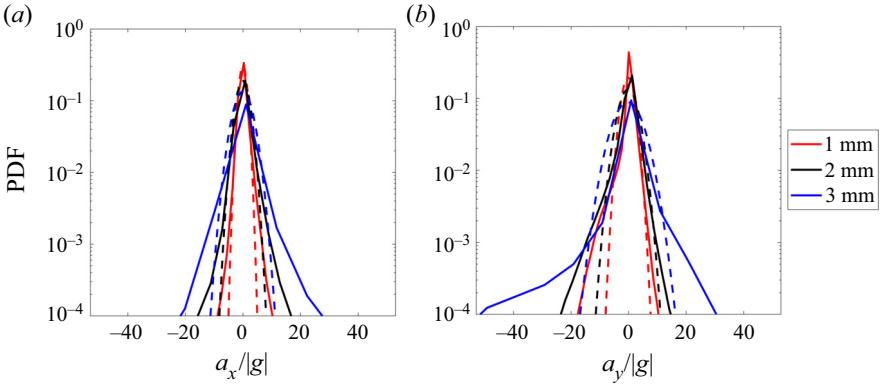

Figure 16. Acceleration component distributions shown with respective Gaussian distributions (dashed lines) with the same mean and standard deviation as experimental curves. (*a*) Horizontal and (*b*) vertical, both normalized by gravity (negative values indicate downward accelerations).

formal distinction between the stable and fluttering mode is not attempted here, the JPDFs suggest that the latter is only statistically significant for the 3 mm disks.

The example in figure 5 suggests that the tumbling occurs with an approximately constant rotation rate. This is confirmed in figure 19, in which various metrics to describe the rotational frequency are considered for the 2 mm case (representative of all tumbling disks in this study). Figure 19(*a*) shows PDFs of $f_t = \omega_t/(2\pi)$ for all instantaneous realizations, as well as the trajectory averaged $\overline{f}_t = \overline{|\omega_t|}/(2\pi)$. The distribution of $f_\theta = 1/(2t_{\theta=0})$ is also plotted, where $t_{\theta=0}$ is the time elapsed between successive changes of sign of θ along each trajectory. The three distributions are sharply peaked around 36 Hz. This is consistent with the behaviour of the Lagrangian temporal autocorrelation of p_x,

$$R^L_{p_x}(\tau) = \frac{\langle p'_x(t+\tau)p'_x(t)\rangle}{\sigma^2_{p_x}(\tau)}, \tag{3.4}$$

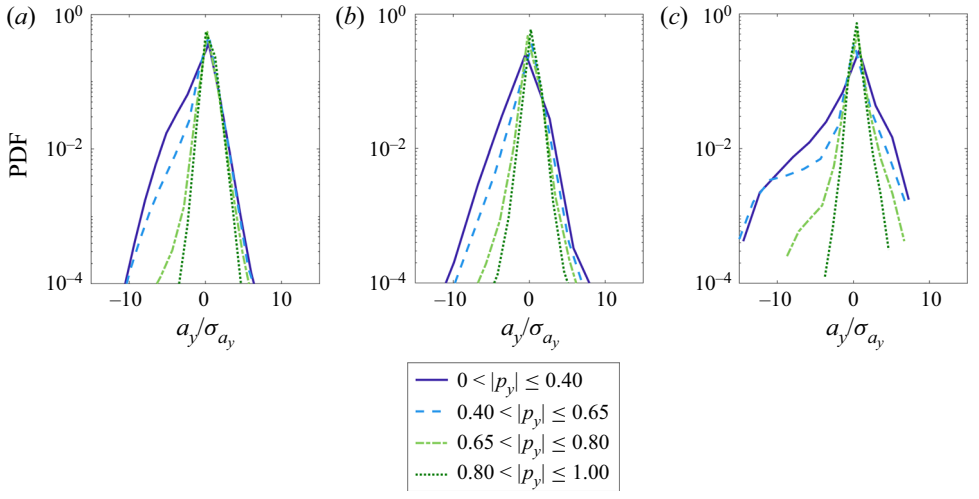

Figure 17. Instantaneous vertical acceleration distributions of tumbling disks normalized by standard deviation of the entire dataset for each respective disk size. Curves separated by ranges of $|p_y|$ going from edge-on orientation ($|p_y| = 0$), shown in solid dark blue, to flat falling orientation ($|p_y| = 1$), shown in dotted dark green. Results are shown for the (*a*) 1 mm, (*b*) 2 mm and (*c*) 3 mm disks. Negative values indicate downward accelerations.

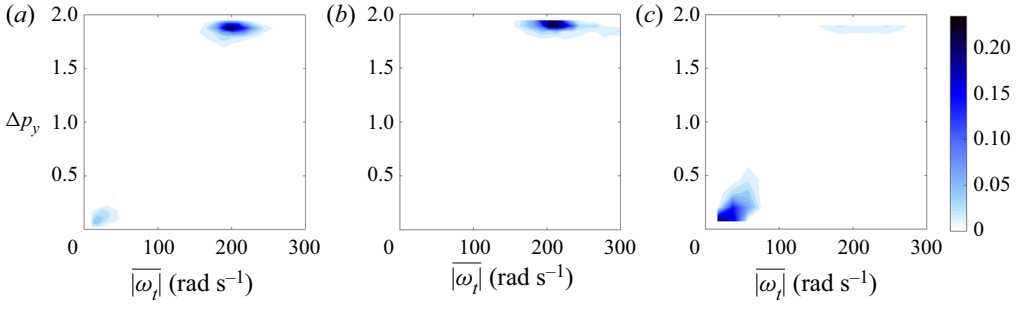

Figure 18. The JPDF of Δp_y values versus trajectory-averaged angular velocity for long trajectories of (*a*) 1 mm, (*b*) 2 mm and (*c*) 3 mm disks.

and of p_y,

$$R^L_{p_y}(\tau) = \frac{\langle p'_y(t+\tau)p'_y(t)\rangle}{\sigma^2_{p_y}(\tau)}, \tag{3.5}$$

where p'_x and p'_y are the fluctuating p-component values calculated as $p'_i = p_i - \overline{p}_i$, $\sigma^2_{p_i}$ is the variance, τ is the temporal abscissa and t is its generic origin (Mordant, Lévêque & Pinton 2004*b*; Guala *et al.* 2007). The mean and variance are both taken as the respective quantity of each individual trajectory. Only trajectories 150 frames and longer are used and all trajectories longer than that are trimmed to 150 frames. Both autocorrelations are plotted in figure 19(*b*), implying an oscillatory behaviour with a characteristic time scale ∼27 ms, in close agreement with the inverse of the dominant frequency in figure 19(*a*).

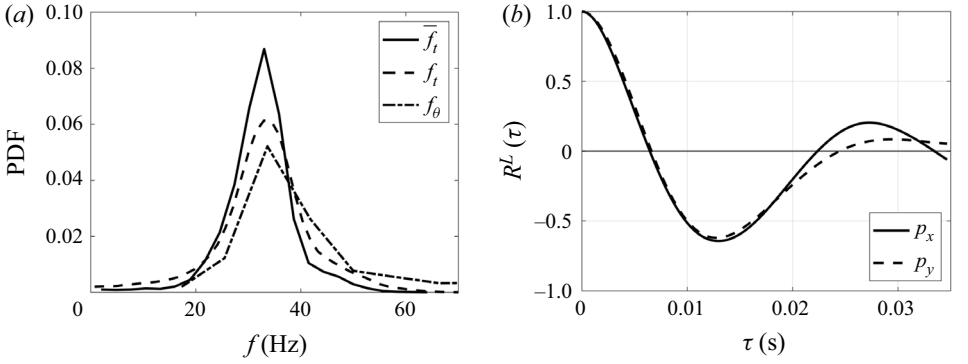

Figure 19. All curves plotted for the 2 mm disks only. (*a*) Tumbling frequency comparison between distributions of instantaneous angular velocity, trajectory-averaged angular velocity and frequency of θ sign changes along a trajectory. (*b*) Lagrangian temporal autocorrelation of p_x and p_y. Secondary peak occurs at 0.027 s, corresponding to 36.4 Hz.

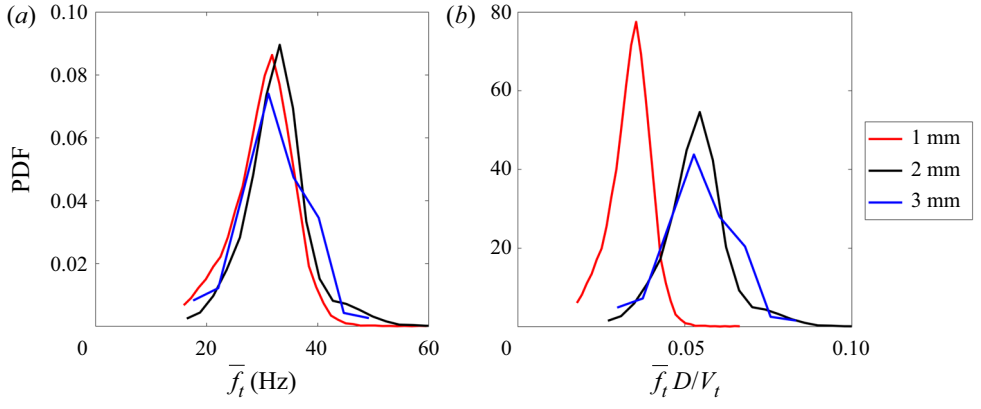

Figure 20. (*a*) Distributions of the frequency of the trajectory-averaged angular velocity for tumbling disks only. (*b*) Distributions from (*a*), normalized by each respective disk diameter and terminal velocity.

The distributions of $\overline{f}_t$ for the tumbling disks are compared in figure 20(*a*), displaying remarkably similar values of the dominant tumbling frequency irrespective of disk size. A common non-dimensionalization of the rotation rate is in the form of a Strouhal number $St = f_t D/V_t$ (Ern *et al.* 2012); see figure 20(*b*). Numerical studies of falling disks and oblate spheroids in the tumbling regime found *St* to increase with *Re* (or *Ga*) (Fernandes *et al.* 2007; Chrust *et al.* 2013), consistent with the present observation. However, those simulations reported significantly larger values ($St = 0.1$–0.4) compared with what is observed here ($St = 0.03$–0.06). This suggests that, in the present range of parameters, the tumbling rate is not set by the wake shedding frequency (which for blunt bodies is expected to yield $St = O(10^{-1})$).

An alternative, *a priori* scaling for the tumbling period can be derived from the dynamic equilibrium between drag and gravity. Within numerical prefactors of order unity

(including the drag coefficient) and considering that $\rho_d \gg \rho_f$, the force balance reads

$$\rho_f U^2 A \sim \rho_d A h g, \tag{3.6}$$

which defines the settling velocity scale $U = \sqrt{\tilde{\rho} h g}$ (as in Belmonte *et al.* (1998) and Mahadevan *et al.* (1999), and analogous to U_g within a factor $\sqrt{2}$). In writing (3.6), we have assumed Newtonian drag scaling (i.e. C_D independent of U and of order unity), which is supported by the results in § 3.2. Then, a characteristic time scale of the motion is given by $\tau_t = U/g = \sqrt{\tilde{\rho} h/g}$. In our experiments, $\tau_t = 76$ ms independent of the disk diameter. This formulation is similar to the classic relation for the response time of spherical particles falling in a quiescent fluid, $\tau_t = V_t/g$. While such a scaling is derived for the linear motion, the translational and rotational dynamics are intimately related and are expected to be governed by similar time scales (Voth & Soldati 2017). The observation that $f_t \tau_t = O(1)$ for all considered disks lends support to the argument that τ_t is the time scale that determines the rotational frequency of tumbling disks in free fall, at least in the considered portion of the parameter space. We note that Mahadevan *et al.* (1999) used a similar argument based on the gravity-drag balance to estimate the rotation rate of falling plates. However, their experiments (conducted at much higher Re and smaller I^*) supported the kinematic relation $U \sim \omega_t D$, i.e. $\omega_t \sim \sqrt{\tilde{\rho} h g/D}$, which does not reflect our observations.

The common scaling for the tumbling frequency of falling bodies, $St \sim \text{const.} = O(10^{-1})$, is associated with a strong coupling between the particle kinematics and the vortex shedding in its wake (Ern *et al.* 2012; Mathai *et al.* 2020). This, however, is mostly based on observations at low $\tilde{\rho}$, where the fluid momentum is comparable to or higher than the particle momentum. In the present range of Re, the wake is expected to shed vortices at a non-dimensional frequency comparable to those studies; but the fluid linear and angular momentum is not sufficient to drive the particle rotation, as signalled by the relatively high $\tilde{\rho}$ and I^*. Rather, the tumbling frequency appears set by the dominant particle inertia and the resulting drag-gravity balance. Nevertheless, oscillations in the wake may still provide the initial seed to trigger tumbling; thus, future work should focus on similar $\tilde{\rho}$ and lower Re, and explore the stable-to-tumbling transition. This is experimentally challenging, as it requires capturing the orientation and rotation of sub-millimetre disks falling in air.

The fact that the 2 mm disks are the most prone to tumbling may indicate that Re and I^* have competing effects in this regard. Indeed, in the present range of parameters, the respective influence of fluid inertia and particle inertia in triggering, sustaining or resisting tumbling is not trivial. It is likely that a threshold Re must be exceeded to incept rotation; but the increase of complexity and loss of coherence in the wake at higher Re may stabilize the motion. Likewise, while fluid forces cannot impose tumbling to particles with asymptotically large I^*, a minimum rotational inertia of the object appears necessary to maintain autorotation. These considerations shall be tested with a comprehensive scanning of the parameter space.

4. Conclusions

We have reported on an experimental study of thin, millimetre-sized disks falling in quiescent air. The considered range of non-dimensional parameters, $\chi = 25{-}60$, $Re = O(10^2)$ and $I^* = O(1)$, is relevant to the settling of snow plate crystals in the atmosphere and to several other natural and industrial processes; still, to our knowledge, it was not systematically investigated before in laboratory experiments. We did not attempt

to scan the parameter space, but rather expanded the number of realizations for each considered case in order to achieve a statistical description of the process.

The falling style emerges as a non-trivial outcome of the input parameters. The 1 and 3 mm disks exhibit bimodal behaviour: either falling approximately stably and flat or tumbling with a fairly invariant rotation rate. Virtually all 2 mm disks tumble. The tendency to tumble is not monotonic with any of the non-dimensional parameters explored, signalling the complexity of the phase diagram. The bimodal behaviour, recently highlighted in numerical studies of both spherical and non-spherical settling particles, underscores the importance of obtaining a large number of realizations to statistically describe the process. The lateral drift during tumbling is stronger for the larger disks. This is explained by the fact that smaller disks have smaller χ and, thus, larger I^*, implying a lesser impact of the aerodynamic torque. Rotational lift is much smaller than drag for all cases, as indicated by the angle of descent being typically smaller than 20°. The relatively weak lateral motion prevents the clear identification of the fluttering mode.

We remark that, in the atmospheric science literature, $Re \approx 100$ is often quoted as a threshold below which plate crystals fall steadily. This is, however, usually assumed when (or deduced by) observing frozen cloud properties via remote sensing (Bréon & Dubrulle 2004; Noel & Chepfer 2004). The present study does not conform to this view, in that the 1 mm disks ($Re = 96$) have a much stronger tendency to tumble than the 3 mm disks ($Re = 360$). Clearly, both Re and I^* play important roles in determining the predominant falling style. The fact that all 2 mm disks tumble, while most of the 3 mm disks do not, suggest sharp transitions in the considered region of the phase diagram. This is to be investigated by a refined exploration of the parameter space that is outside the scope of this work.

We observe larger fall speeds than what is predicted by existing correlations based on experiments in liquids. Those are limited to much smaller I^* compared with the present study, and their results have been typically parameterized based on Re (or Ga) alone. Our measurements instead stress how the density ratio is consequential not only for the rotational dynamics but also for settling, especially in the considered regime in which fluid inertia is relatively large. Indeed, the departure of our observations from those correlations increases with Re. For the disks exhibiting bimodal behaviour, tumbling and non-tumbling instances show different settling velocities. Surprisingly, the trend is different for the 1 and 3 mm disks, the former falling faster when tumbling and the latter falling slower. This may be due to qualitative differences in the wake behaviour at the different Re, yielding different coupling with the disk motion. This remains speculative without direct observation of the wake dynamics, whose details are below the achievable spatial resolution. Fully resolved simulations are warranted to elucidate this point.

Tumbling disks experience intense instantaneous accelerations during the phase of motion in which they fall edge-on. Still, the classic definition of drag coefficient, based on the steady-state force balance of flat falling disks, provide a fair statistical estimate for the instantaneous behaviour. Assuming similar time scales for the rotational and translational motion, we then deduce a scaling of the tumbling period $\sim \sqrt{\tilde{\rho} h/g}$. This approximately agrees with the observed rotation rate and its independence with disk diameter, and shall be tested in future studies varying density ratio and disk thickness.

The regime we have considered is challenging to capture numerically, and some of the important dynamics may not be represented by previous experiments in liquids. Therefore, besides providing direct insight on the fundamental particle–fluid interaction, we believe

the data represent a useful test case for validation. Further studies shall address open questions concerning the influence of different physical parameters. In particular, three directions appear especially interesting and potentially fruitful. First, the diameter range can be expanded, towards both smaller and larger sizes. Recent numerical studies have focused on sub-millimetre objects (e.g. Jucha *et al.* 2018), and a direct comparison may shed light on dynamics that can hardly be resolved in experiments such as those presented here. This would also allow probing deeper below the threshold $Re = 100$, whose strict validity has been questioned here. On the other hand, considering larger disks would allow testing the high-Ga end of the parameter space in figure 1, and verify whether an asymptotic behaviour is reached or whether different dynamics arise. Second, in order to more efficiently probe the parameter space, one may vary the disk material and geometry independently. This would enable the independent variation of I^* and Ga, while both have been varied simultaneously in the present study. Third and finally, it would be desirable to use lightweight materials that more closely replicate the bulk density of frozen hydrometeors, which for complex shapes is far below the one of ice (Pruppacher & Klett 2010). This would allow focusing on regimes most relevant for atmospheric science, especially if such materials were used in additive manufacturing, so as to replicate complex shapes found in frozen precipitation.

The effect of plate shape on the falling style has been highlighted by recent experiments at low $\tilde{\rho}$ (Esteban *et al.* 2018; Vincent, Liu & Kanso 2020) and deserves to be explored at high $\tilde{\rho}$, especially in the context of the settling of frozen hydrometeors. The latter is expected to be crucially influenced by atmospheric turbulence, as recently documented by the numerical studies of Jucha *et al.* (2018), Gustavsson *et al.* (2021) and Sheikh *et al.* (2022) for sub-millimetre plate crystals. The effect of air turbulence on millimetre-sized disks similar to those investigated here will be the subject of a future study.

Acknowledgements. F.C. is thankful to U. Lohmann and J. Henneberger (Institute for Atmospheric and Climate Science, ETH Zürich) for several insightful discussions on frozen precipitation.

Funding. This work was supported by the US National Science Foundation (Physical and Dynamic Meteorology program) through grant NSF-AGS-1822192.

Declaration of interests. The authors report no conflict of interest.

Author ORCIDs.
Amy Tinklenberg https://orcid.org/0000-0003-3121-3183;
Michele Guala https://orcid.org/0000-0002-9788-8119;
Filippo Coletti https://orcid.org/0000-0001-5344-2476.

Appendix

The quantities presented in § 3, obtained at volume fractions $\Phi_V = O(10^{-5})$, are not significantly different when measured at $\Phi_V = O(10^{-6})$. For brevity, this is shown for exemplary quantities for the 2 mm disks and, in particular, the histogram of Δp_y (figure 21*a*,*b*), the PDF a_y (figure 21*c*) and the PDF of $|\omega_t|$ (figure 21*d*). The fact that virtually all 2 mm disks tumble, irrespective of the volume fraction, indicates this is not the effect of air disturbance due to the wakes of other falling disks. This supports the claim that the objects are dilute enough to exert negligible mutual interaction.

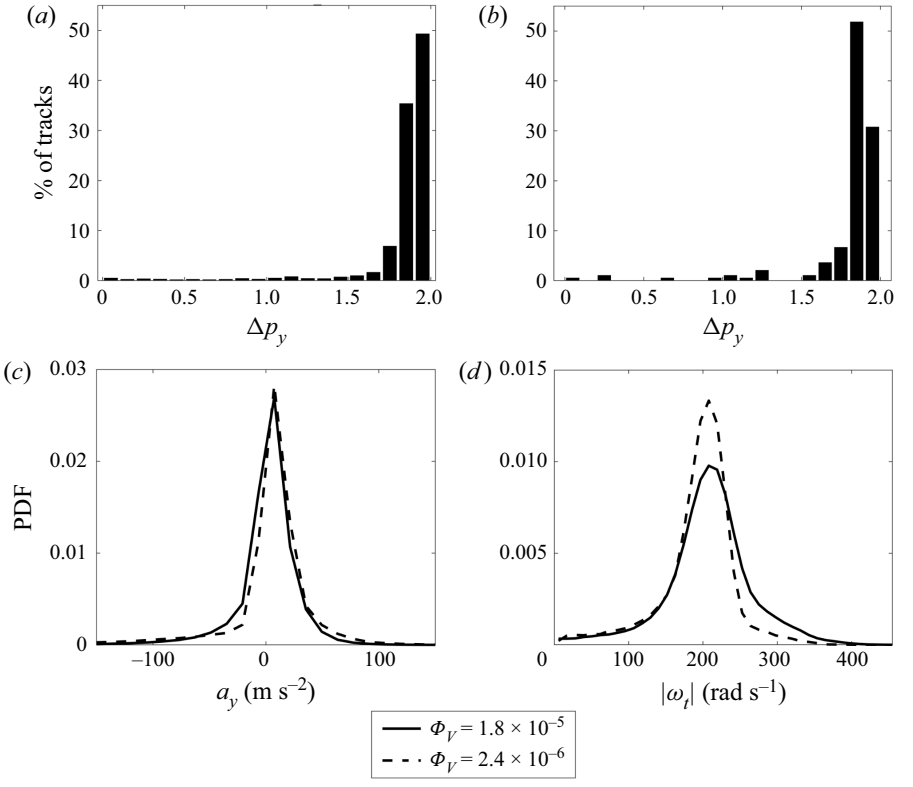

Figure 21. Statistical comparison between two experiments performed using the 2 mm diameter disks dispersed at different volume fractions. (*a*) Histogram of p_y range for $\Phi_V = 1.8 \times 10^{-5}$ (as in figure 7*b*), compared with (*b*) for $\Phi_V = 2.4 \times 10^{-6}$. In (*c*) and (*d*) the solid lines indicate the volume fraction that is presented in the results of this paper, while dashed lines indicate a more dilute volume fraction tested, showing (*c*) the instantaneous vertical acceleration distribution and (*d*) the instantaneous angular velocity distribution.

References

Alméras, E., Mathai, V., Lohse, D. & Sun, C. 2017 Experimental investigation of the turbulence induced by a bubble swarm rising within incident turbulence. *J. Fluid Mech.* **825**, 1091–1112.

Andersen, A., Pesavento, U. & Wang, Z.J. 2005 Unsteady aerodynamics of fluttering and tumbling plates. *J. Fluid Mech.* **541**, 65–90.

Auer, A.H. & Veal, D.L. 1970 The dimension of ice crystals in natural clouds. *J. Atmos. Sci.* **27** (6), 919–926.

Auguste, F., Magnaudet, J. & Fabre, D. 2013 Falling styles of disks. *J. Fluid Mech.* **719**, 388–405.

Bagheri, G. & Bonadonna, C. 2016 On the drag of freely falling non-spherical particles. *Powder Technol.* **301**, 526–544.

Baker, L.J. 2021 Experimental investigation of inertial sphere, rod, and disk particles in a turbulent boundary layer. PhD thesis, University of Minnesota.

Baker, L.J. & Coletti, F. 2022 Experimental investigation of inertial fibres and disks in a turbulent boundary layer. *J. Fluid Mech.* **943**, A27.

Barthazy, E. & Schefold, R. 2006 Fall velocity of snowflakes of different riming degree and crystal types. *Atmos. Res.* **82** (1), 391–398.

Belmonte, A., Eisenberg, H. & Moses, E. 1998 From flutter to tumble: inertial drag and Froude similarity in falling paper. *Phys. Rev. Lett.* **81** (2), 345–348.

Berk, T. & Coletti, F. 2021 Dynamics of small heavy particles in homogeneous turbulence: a Lagrangian experimental study. *J. Fluid Mech.* **917**, A47.

Bodenschatz, E., Malinowski, S.P., Shaw, R.A. & Stratmann, F. 2010 Can we understand clouds without turbulence? *Science* **327** (5968), 970–971.

BÖHM, H.P. 1989 A general equation for the terminal fall speed of solid hydrometeors. *J. Atmos. Sci.* **46** (15), 2419–2427.

BRANDT, L. & COLETTI, F. 2022 Particle-laden turbulence: progress and perspectives. *Annu. Rev. Fluid Mech.* **54** (1), 159–189.

BRÉON, F.-M. & DUBRULLE, B. 2004 Horizontally oriented plates in clouds. *J. Atmos. Sci.* **61** (23), 2888–2898.

BROWN, P.P. & LAWLER, D.F. 2003 Sphere drag and settling velocity revisited. *J. Environ. Engng* **129** (3), 222–231.

CABRERA, F.E. 2021 Settling of particles in quiescent and turbulent flows. From ground conditions to micro-gravity. Theses, Université de Lyon.

CARTER, D.W. & COLETTI, F. 2017 Scale-to-scale anisotropy in homogeneous turbulence. *J. Fluid Mech.* **827**, 250–284.

CARTER, D.W. & COLETTI, F. 2018 Small-scale structure and energy transfer in homogeneous turbulence. *J. Fluid Mech.* **854**, 505–543.

CARTER, D., PETERSEN, A., AMILI, O. & COLETTI, F. 2016 Generating and controlling homogeneous air turbulence using random jet arrays. *Exp. Fluids* **57** (12), 189.

CHENG, K.-Y., WANG, P.K. & HASHINO, T. 2015 A numerical study on the attitudes and aerodynamics of freely falling hexagonal ice plates. *J. Atmos. Sci.* **72** (9), 3685–3698.

CHRUST, M., BOUCHET, G. & DUŠEK, J. 2013 Numerical simulation of the dynamics of freely falling discs. *Phys. Fluids* **25** (4), 044102.

EBRAHIMIAN, M., SEAN SANDERS, R. & GHAEMI, S. 2019 Dynamics and wall collision of inertial particles in a solid–liquid turbulent channel flow. *J. Fluid Mech.* **881**, 872–905.

ELOY, C., SOUILLIEZ, C. & SCHOUVEILER, L. 2007 Flutter of a rectangular plate. *J. Fluids Struct.* **23** (6), 904–919.

ERN, P., RISSO, F., FABRE, D. & MAGNAUDET, J. 2012 Wake-induced oscillatory paths of bodies freely rising or falling in fluids. *Annu. Rev. Fluid Mech.* **44** (1), 97–121.

ESTEBAN, L.B., SHRIMPTON, J. & GANAPATHISUBRAMANI, B. 2018 Edge effects on the fluttering characteristics of freely falling planar particles. *Phys. Rev. Fluids* **3** (6), 064302.

ESTEBAN, L.B., SHRIMPTON, J.S. & GANAPATHISUBRAMANI, B. 2020 Disks settling in turbulence. *J. Fluid Mech.* **883**, A58.

FABRE, D., ASSEMAT, P. & MAGNAUDET, J. 2011 A quasi-static approach to the stability of the path of heavy bodies falling within a viscous fluid. *J. Fluids Struct.* **27** (5–6), 758–767.

FERNANDES, P.C., RISSO, F., ERN, P. & MAGNAUDET, J. 2007 Oscillatory motion and wake instability of freely rising axisymmetric bodies. *J. Fluid Mech.* **573**, 479–502.

FIELD, S.B., KLAUS, M., MOORE, M.G. & NORI, F. 1997 Chaotic dynamics of falling disks. *Nature* **388** (6639), 252–254.

FORNARI, W., ARDEKANI, M.N. & BRANDT, L. 2018 Clustering and increased settling speed of oblate particles at finite Reynolds number. *J. Fluid Mech.* **848**, 696–721.

GARRETT, T.J. & YUTER, S.E. 2014 Observed influence of riming, temperature, and turbulence on the fallspeed of solid precipitation. *Geophys. Res. Lett.* **41** (18), 6515–6522.

GERASHCHENKO, S., SHARP, N.S., NEUSCAMMAN, S. & WARHAFT, Z. 2008 Lagrangian measurements of inertial particle accelerations in a turbulent boundary layer. *J. Fluid Mech.* **617**, 255–281.

GUALA, M., LIBERZON, A., TSINOBER, A. & KINZELBACH, W. 2007 An experimental investigation on Lagrangian correlations of small-scale turbulence at low Reynolds number. *J. Fluid Mech.* **574**, 405–427.

GUSTAVSSON, K., SHEIKH, M.Z., NASO, A., PUMIR, A. & MEHLIG, B. 2021 Effect of particle inertia on the alignment of small ice crystals in turbulent clouds. *J. Atmos. Sci.* **78** (8), 2573–2587.

HEISINGER, L., NEWTON, P. & KANSO, E. 2014 Coins falling in water. *J. Fluid Mech.* **742**, 243–253.

HEYMSFIELD, A.J. & WESTBROOK, C.D. 2010 Advances in the estimation of ice particle fall speeds using laboratory and field measurements. *J. Atmos. Sci.* **67** (8), 2469–2482.

HIGUCHI, K. 1956 A new method for the simultaneous observation of shape and size of a large number of falling snow particles. *J. Atmos. Sci.* **13** (3), 274–278.

HONG, S.-Y., DUDHIA, J. & CHEN, S.-H. 2004 A revised approach to ice microphysical processes for the bulk parameterization of clouds and precipitation. *Mon. Weath. Rev.* **132** (1), 103–120.

HUISMAN, S.G., BAROIS, T., BOURGOIN, M., CHOUIPPE, A., DOYCHEV, T., HUCK, P., MORALES, C.E.B., UHLMANN, M. & VOLK, R. 2016 Columnar structure formation of a dilute suspension of settling spherical particles in a quiescent fluid. *Phys. Rev. Fluids* **1** (7), 074204.

IPCC 2021 Climate change 2021: the physical science basis. Contribution of working group I to the sixth assessment report of the intergovernmental panel on climate change. Cambridge University Press.

JAYAWEERA, K.O.L.F. 1965 The behaviour of small clusters of bodies falling in a viscous fluid. PhD thesis, Imperial College London.

JAYAWEERA, K.O.L.F. 1972 An equivalent disc for calculating the terminal velocities of plate-like ice crystals. *J. Atmos. Sci.* **29** (3), 596–598.

JAYAWEERA, K.O.L.F. & COTTIS, R.E. 1969 Fall velocities of plate-like and columnar ice crystals. *Q. J. R. Meteorol. Soc.* **95** (406), 703–709.

JENNY, M., DUEK, J. & BOUCHET, G. 2004 Instabilities and transition of a sphere falling or ascending freely in a Newtonian fluid. *J. Fluid Mech.* **508**, 201–239.

JONES, M.A. & SHELLEY, M.J. 2005 Falling cards. *J. Fluid Mech.* **540**, 393–425.

JUCHA, J., NASO, A., LÉVÊQUE, E. & PUMIR, A. 2018 Settling and collision between small ice crystals in turbulent flows. *Phys. Rev. Fluids* **3** (1), 014604.

KAJIKAWA, M. 1971 A model experimental study on the falling velocity of ice crystals. *J. Met. Soc. Japan. Ser. II* **49** (5), 367–375.

KAJIKAWA, M. 1972 Measurement of falling velocity of individual snow crystals. *J. Met. Soc. Japan. Ser. II* **50** (6), 577–584.

KAJIKAWA, M. 1975 Experimental formula of falling velocity of snow crystals. *J. Met. Soc. Japan. Ser. II* **53** (4), 267–275.

KAJIKAWA, M. 1992 Observations of the falling motion of plate-like snow crystals part I: the free-fall patterns and velocity. *J. Met. Soc. Japan. Ser. II* **70** (1), 1–9.

KHVOROSTYANOV, V.I. & CURRY, J.A. 2002 Terminal velocities of droplets and crystals: power laws with continuous parameters over the size spectrum. *J. Atmos. Sci.* **59** (11), 1872–1884.

LAU, E.M., HUANG, W.-X. & XU, C.-X. 2018 Progression of heavy plates from stable falling to tumbling flight. *J. Fluid Mech.* **850**, 1009–1031.

LAUBER, A., HENNEBERGER, J., MIGNANI, C., RAMELLI, F., PASQUIER, J.T., WIEDER, J., HERVO, M. & LOHMANN, U. 2021 Continuous secondary-ice production initiated by updrafts through the melting layer in mountainous regions. *Atmos. Chem. Phys.* **21** (5), 3855–3870.

LEHNING, M., LÖWE, H., RYSER, M. & RADERSCHALL, N. 2008 Inhomogeneous precipitation distribution and snow transport in steep terrain. *Water Resour. Res.* **44** (7), W07404.

LI, J., ABRAHAM, A., GUALA, M. & HONG, J. 2021 Evidence of preferential sweeping during snow settling in atmospheric turbulence. *J. Fluid Mech.* **928**, A8.

LIST, R. & SCHEMENAUER, R.S. 1971 Free-fall behavior of planar snow crystals, conical graupel and small hail. *J. Atmos. Sci.* **28** (1), 110–115.

MAHADEVAN, L., RYU, W.S. & SAMUEL, A.D.T. 1999 Tumbling cards. *Phys. Fluids* **11** (1), 1–3.

MATHAI, V., HUISMAN, S.G., SUN, C., LOHSE, D. & BOURGOIN, M. 2018 Dispersion of air bubbles in isotropic turbulence. *Phys. Rev. Lett.* **121** (5), 054501.

MATHAI, V., LOHSE, D. & SUN, C. 2020 Bubbly and buoyant particle-laden turbulent flows. *Annu. Rev. Condens. Matter Phys.* **11** (1), 529–559.

MATHAI, V., NEUT, M.W.M., VAN DER POEL, E.P. & SUN, C. 2016 Translational and rotational dynamics of a large buoyant sphere in turbulence. *Exp. Fluids* **57** (4), 51.

MATHAI, V., ZHU, X., SUN, C. & LOHSE, D. 2017 Mass and moment of inertia govern the transition in the dynamics and wakes of freely rising and falling cylinders. *Phys. Rev. Lett.* **119** (5), 054501.

MATROSOV, S.Y., REINKING, R.F., KROPFLI, R.A., MARTNER, B.E. & BARTRAM, B.W. 2001 On the use of radar depolarization ratios for estimating shapes of ice hydrometeors in winter clouds. *J. Appl. Meteorol.* **40** (3), 479–490.

MCCORQUODALE, M.W. & WESTBROOK, C.D. 2021*a* TRAIL: a novel approach for studying the aerodynamics of ice particles. *Q. J. R. Meteorol. Soc.* **147** (734), 589–604.

MCCORQUODALE, M.W. & WESTBROOK, C.D. 2021*b* TRAIL part 2: a comprehensive assessment of ice particle fall speed parametrisations. *Q. J. R. Meteorol. Soc.* **147** (734), 605–626.

MITCHELL, D.L. 1996 Use of mass- and area-dimensional power laws for determining precipitation particle terminal velocities. *J. Atmos. Sci.* **53** (12), 1710–1723.

MITTAL, R., SESHADRI, V. & UDAYKUMAR, H.S. 2004 Flutter, tumble and vortex induced autorotation. *Theor. Comput. Fluid Dyn.* **17** (3), 165–170.

MORDANT, N., CRAWFORD, A.M. & BODENSCHATZ, E. 2004*a* Three-dimensional structure of the Lagrangian acceleration in turbulent flows. *Phys. Rev. Lett.* **93** (21), 214501.

MORDANT, N., LÉVÊQUE, E. & PINTON, J.-F. 2004*b* Experimental and numerical study of the Lagrangian dynamics of high Reynolds turbulence. *New J. Phys.* **6**, 116.

MORICHE, M., UHLMANN, M. & DUŠEK, J. 2021 A single oblate spheroid settling in unbounded ambient fluid: a benchmark for simulations in steady and unsteady wake regimes. *Intl J. Multiphase Flow* **136**, 103519.

NAMKOONG, K., YOO, J.Y. & CHOI, H.G. 2008 Numerical analysis of two-dimensional motion of a freely falling circular cylinder in an infinite fluid. *J. Fluid Mech.* **604**, 33–53.

NEMES, A., DASARI, T., HONG, J., GUALA, M. & COLETTI, F. 2017 Snowflakes in the atmospheric surface layer: observation of particle–turbulence dynamics. *J. Fluid Mech.* **814**, 592–613.

NOEL, V. & CHEPFER, H. 2004 Study of ice crystal orientation in cirrus clouds based on satellite polarized radiance measurements. *J. Atmos. Sci.* **61** (16), 2073–2081.

ONO, A. 1969 The shape and riming properties of ice crystals in natural clouds. *J. Atmos. Sci.* **26** (1), 138–147.

PESAVENTO, U. & WANG, Z.J. 2004 Falling paper: Navier–Stokes solutions, model of fluid forces, and center of mass elevation. *Phys. Rev. Lett.* **93** (14), 144501.

PETERSEN, A.J., BAKER, L. & COLETTI, F. 2019 Experimental study of inertial particles clustering and settling in homogeneous turbulence. *J. Fluid Mech.* **864**, 925–970.

PRUPPACHER, H.R. & KLETT, J.D. 2010 *Microphysics of Clouds and Precipitation*. Kluwer Academic Publishers.

RAAGHAV, S.K.R., POELMA, C. & BREUGEM, W.-P. 2022 Path instabilities of a freely rising or falling sphere. *Intl J. Multiphase Flow* **153**, 104111.

RADENZ, M., BÜHL, J., SEIFERT, P., GRIESCHE, H. & ENGELMANN, R. 2019 peakTree: a framework for structure-preserving radar Doppler spectra analysis. *Atmos. Meas. Tech.* **12** (9), 4813–4828.

RIBOUX, G., RISSO, F. & LEGENDRE, D. 2010 Experimental characterization of the agitation generated by bubbles rising at high Reynolds number. *J. Fluid Mech.* **643**, 509–539.

RISSO, F. 2018 Agitation, mixing, and transfers induced by bubbles. *Annu. Rev. Fluid Mech.* **50** (1), 25–48.

ROHATGI, A. 2021 WebPlotDigitizer.

ROSCOE, R. 1949 XXXI. The flow of viscous fluids round plane obstacles. *Lond. Edinb. Dubl. Phil. Mag. J. Sci.* **40** (302), 338–351.

ROSENDAHL, L. 2000 Using a multi-parameter particle shape description to predict the motion of non-spherical particle shapes in swirling flow. *Appl. Math. Model* **24** (1), 11–25.

SASSEN, K. 1980 Remote sensing of planar ice crystal fall attitudes. *J. Met. Soc. Japan. Ser. II* **58** (5), 422–429.

SHEIKH, M.Z., GUSTAVSSON, K., LÉVÊQUE, E., MEHLIG, B., PUMIR, A. & NASO, A. 2022 Colliding ice crystals in turbulent clouds. *J. Atmos. Sci.* **79** (9), 2205–2218.

TAGLIAVINI, G., MCCORQUODALE, M., WESTBROOK, C., CORSO, P., KROL, Q. & HOLZNER, M. 2021*a* Drag coefficient prediction of complex-shaped snow particles falling in air beyond the Stokes regime. *Intl J. Multiphase Flow* **140**, 103652.

TAGLIAVINI, G., MCCORQUODALE, M., WESTBROOK, C. & HOLZNER, M. 2021*b* Numerical analysis of the wake of complex-shaped snow particles at moderate Reynolds number. *Phys. Fluids* **33** (10), 105103.

TOUPOINT, C., ERN, P. & ROIG, V. 2019 Kinematics and wake of freely falling cylinders at moderate Reynolds numbers. *J. Fluid Mech.* **866**, 82–111.

UHLMANN, M. & DOYCHEV, T. 2014 Sedimentation of a dilute suspension of rigid spheres at intermediate Galileo numbers: the effect of clustering upon the particle motion. *J. Fluid Mech.* **752**, 310–348.

VINCENT, L., LIU, Y. & KANSO, E. 2020 Shape optimization of tumbling wings. *J. Fluid Mech.* **889**, A9.

VOTH, G.A., LA PORTA, A., CRAWFORD, A.M., ALEXANDER, J. & BODENSCHATZ, E. 2002 Measurement of particle accelerations in fully developed turbulence. *J. Fluid Mech.* **469**, 121–160.

VOTH, G.A. & SOLDATI, A. 2017 Anisotropic particles in turbulence. *Annu. Rev. Fluid Mech.* **49** (1), 249–276.

WANG, P.K. 2021 Observational studies of ice hydrometeors and their fall behavior. In *Motions of Ice Hydrometeors in the Atmosphere: Numerical Studies and Implications*. Springer.

WESTBROOK, C.D. & SEPHTON, E.K. 2017 Using 3-D-printed analogues to investigate the fall speeds and orientations of complex ice particles. *Geophys. Res. Lett.* **44** (15), 7994–8001.

WILLMARTH, W.W., HAWK, N.E. & HARVEY, R.L. 1964 Steady and unsteady motions and wakes of freely falling disks. *Phys. Fluids* **7** (2), 197–208.

YIN, C., ROSENDAHL, L., KNUDSEN KÆR, S. & SØRENSEN, H. 2003 Modelling the motion of cylindrical particles in a nonuniform flow. *Chem. Engng Sci.* **58** (15), 3489–3498.

ZASTAWNY, M., MALLOUPPAS, G., ZHAO, F. & VAN WACHEM, B. 2012 Derivation of drag and lift force and torque coefficients for non-spherical particles in flows. *Intl J. Multiphase Flow* **39**, 227–239.

ZHONG, H., CHEN, S. & LEE, C. 2011 Experimental study of freely falling thin disks: transition from planar zigzag to spiral. *Phys. Fluids* **23** (1), 011702.

ZIMMERMANN, R., GASTEUIL, Y., BOURGOIN, M., VOLK, R., PUMIR, A. & PINTON, J.-F. 2011 Rotational intermittency and turbulence induced lift experienced by large particles in a turbulent flow. *Phys. Rev. Lett.* **106** (15), 154501.